Monthly Notices of the ROYAL ASTRONOMICAL SOCIETY

MNRAS **501,** 1394–1412 (2021) doi:10.1093/mnras/staa3712
Advance Access publication 2020 November 28

Radio light curves and imaging of the helium nova V445 Puppis reveal seven years of synchrotron emission

M. M. Nyamai [1]★ L. Chomiuk,[2]★ V. A. R. M. Ribeiro [3,4] P. A. Woudt [1] J. Strader[2] and K. V. Sokolovsky [2,5]

[1]*Department of Astronomy, University of Cape Town, Private Bag X3, Rondebosch 7701, South Africa*
[2]*Department of Physics and Astronomy, Michigan State University, East Lansing, MI 48824, USA*
[3]*Instituto de Telecomunicações, Campus Universitário de Santiago, P-3810-193 Aveiro, Portugal*
[4]*Departamento de Física, Universidade de Aveiro, Campus Universitário de Santiago, P-3810-193 Aveiro, Portugal*
[5]*Sternberg Astronomical Institute, Moscow State University, Universitetskii pr. 13, 119992 Moscow, Russia*

Accepted 2020 November 23. Received 2020 November 23; in original form 2020 August 4

ABSTRACT

V445 Puppis is the only helium nova observed to date; its eruption in late 2000 showed high velocities up to 8500 km s^{-1}, and a remarkable bipolar morphology cinched by an equatorial dust disc. Here we present multifrequency radio observations of V445 Pup obtained with the Very Large Array (VLA) spanning 1.5–43.3 GHz, and between 2001 January and 2008 March (days ∼89–2700 after eruption). The radio light curve is dominated by synchrotron emission over these 7 yr, and shows four distinct radio flares. Resolved radio images obtained in the VLA's A configuration show that the synchrotron emission hugs the equatorial disc, and comparisons to near-IR images of the nova clearly demonstrate that it is the densest ejecta – not the fastest ejecta – that are the sites of the synchrotron emission in V445 Pup. The data are consistent with a model where the synchrotron emission is produced by a wind from the white dwarf impacting the dense equatorial disc, resulting in shocks and particle acceleration. The individual synchrotron flares may be associated with density enhancements in the equatorial disc and/or velocity variations in the wind from the white dwarf. This overall scenario is similar to a common picture of shock production in hydrogen-rich classical novae, but V445 Pup is remarkable in that these shocks persist for almost a decade, much longer than the weeks or months for which shocks are typically observed in classical novae.

Key words: binaries: close – stars: individual: V445 Pup – novae, cataclysmic variables – radio continuum: transients – transients: novae.

1 INTRODUCTION

Extensive accretion of helium-rich material on to a white dwarf (WD) from a helium companion star results in increasing density and temperature on the WD surface, eventually triggering a helium shell flash (known as a helium nova; Kato, Saio & Hachisu 1989). Helium novae occur for mass accretion rates in the range $\sim 10^{-8}$ to 10^{-7} M$_\odot$ yr^{-1} (Woosley & Kasen 2011; Piersanti et al. 2013). The thermonuclear runaway ejects the outer accreted layers analogous to hydrogen-rich classical novae (see e.g. Bode & Evans 2008; Woudt & Ribeiro 2014), although more mass is ejected in helium novae (Kato et al. 1989; Hillman et al. 2016). However, when the helium accretion rate is lower ($\leq 10^{-8}$ M$_\odot$ yr^{-1}), it is possible for a helium ignition on the surface of the WD to trigger an inward shockwave which leads to an explosion at the core of the WD hence a double detonation (Nomoto 1982; Shen & Bildsten 2009). If the detonation occurs on a carbon–oxygen WD, it could produce a Type Ia supernova (SN Ia; Moll & Woosley 2013; Piersanti, Tornambé & Yungelson 2014; Ruiter et al. 2014). The study of helium accretion is therefore important for validating or ruling out helium-donor and WD binary systems as progenitors of SNe Ia.

In this paper, we present radio observations of the only spectroscopically confirmed helium nova, V445 Puppis. The nova was discovered in eruption in late 2000 November at an optical maximum of $V \approx 8.6$ mag (Kato et al. 2000), substantially brighter than its $V \approx 14.5$ pre-eruption magnitude (Ashok & Banerjee 2003). The day of eruption for V445 Pup is unknown and only constrained to be between 2000 September 26 and 2000 November 28 (Kato et al. 2000; Ashok & Banerjee 2001; Woudt et al. 2009). We adopt a t_0 from Woudt et al. (2009) of 2000 November 2 (MJD = 51850) as the time of eruption. The nova was unusually rich in carbon and showed helium emission lines, but lacked hydrogen lines (which are prominent in the spectra of classical novae; Ashok & Banerjee 2003; Iijima & Nakanishi 2008; Woudt et al. 2009).

Within one month of the eruption, dust was detected from the nova using infrared spectroscopy (Lynch et al. 2004). By ∼8 months after the nova eruption, the optical brightness had dropped below pre-eruption levels (Ashok & Banerjee 2003; Woudt et al. 2009), attributed to a strong dust formation episode. Six years following the eruption, the optical light had still not returned to pre-eruption levels (Woudt et al. 2009), and the dust mass was determined to be $> 10^{-5}$ M$_\odot$ (Shimamoto et al. 2017).

V445 Pup was spatially resolved using near-infrared adaptive optics imaging with the Very Large Telescope (VLT), revealing an

★ E-mail: nymmir001@myuct.ac.za (MMN); chomiukl@msu.edu (LC)

Table 1. Log of VLA observations of V445 Pup.

Observation Date	t (MJD)	$t - t_0$ (d)	Configuration	Observation time on target (min)					
				1.43 GHz	4.86 GHz	8.46 GHz	14.94 GHz	22.46 GHz	43.34 GHz
2001 Jan 18	51927	77	A	...	...	3.7	...	...	...
2001 Jan 30	51939	89	A	...	...	6.4	...	...	...
2001 Sept 09	52162	312	C	...	...	6.7	...	...	...
2001 Sept 11	52164	314	C	15.6	3.7	...	5.2	4.6	4.4
2001 Sept 12	52165	315	C	10.9	3.9	3.7	5.2	4.4	...
2001 Sept 14	52167	317	C	...	4.1	...	...	...	...
2001 Sept 15	52168	318	C&D	...	1.9	3.1	...	...	...
2001 Sept 16	52169	319	C&D	5.2	6.9	6.9	4.9	...	...
2001 Sept 17	52170	320	C&D	10.4	11.2	...	11.9	...	...
2001 Sept 20	52173	323	C&D	3.7	4.2	4.2	4.2	4.2	...
2001 Sept 25	52178	328	C&D	...	11.7	12.7	14.8	...	...
2001 Sept 26	52179	329	C&D	...	3.2	4.7	6.2	6.2	...

Note. '...' indicates no observations for this epoch at that frequency. Here, t_0 is taken as 2000 November 2 (MJD = 51850). This table is continued in Appendix C Table C1.

expanding bipolar shell confined by an equatorial dust disc and with polar knots on both ends of the bipolar ejecta (Woudt et al. 2009; see their fig. 2). Woudt et al. (2009) determined a distance of 8.2 ± 0.5 kpc to the nova using expansion parallax techniques.

Presented in this paper are multifrequency observations of the nova obtained in the years following eruption using the Very Large Array (VLA) radio telescope. The radio data reveal an unprecedented, near decade-long, synchrotron-powered radio light curve. In Section 2, we discuss the radio observations and our data analysis procedure. In Section 3, we present the multifrequency radio light curve, radio spectral evolution, and spatially resolved radio imaging. In Section 4, we present the results, and in Section 5 we highlight our conclusions.

2 OBSERVATIONS AND DATA ANALYSIS

Radio observations of V445 Pup were obtained with a variety of VLA programs, most of which were led by M. Rupen. The data were retrieved from the VLA archive (see Table 1 for a log of the observations). The first radio observations of V445 Pup were taken on 2001 January 18 and 30 ($t - t_0 = 77$ and 89 d). On day 77, the nova was not detected at 8.4 GHz (Rupen, Dhawan & Mioduszewski 2001), and there was a marginal detection on day 89. After day 89, observations were paused until 2001 September 9 (day 312), when the nova was strongly detected at 8.4 GHz (Rupen et al. 2001). V445 Pup was subsequently observed with the VLA from 2001 September to 2008 March (between day 312 and 2704), resulting in a detailed radio light curve spanning almost a decade following the eruption (Fig. 1).

Observations were obtained in continuum mode, at different frequency bands with two 50 MHz-wide frequency channels. The observations were conducted at L (1.46 GHz), C (4.86 GHz), X (8.46 GHz), U (14.94 GHz), K (22.46 GHz), and Q (43.34 GHz) bands, and are used to trace the nova emission throughout all of the VLA's configurations. The VLA A configuration provides the highest resolution (synthesized beam FWHM of 2 arcsec at 1.5 GHz and 0.3 arcsec at 8.5 GHz), and has the potential to provide resolved images (see Section 3.3). At each frequency, observations of the target are obtained together with observations of gain calibrators (see Table 2). The most common gain calibrator used was 0804-278, for which we took the ICRS coordinates RA = 08h04m51.451s and Dec = $-27°49'11.32''$. We note that a slightly different RA position was used by National Radio Astronomy Observatory (NRAO) for this calibrator in 2001–2002 (RA = 08h04m51.440s); we, therefore, shifted the data so that all observations take RA = 08h04m51.451s (this is particularly relevant for our imaging results; Section 3.3). Flux density calibrators 0137 + 331 (3C 48), 0542 + 498 (3C 147) or 1331 + 305 (3C 286) were observed to set the absolute flux density scale. Some observations were obtained without a flux density calibrator; in most cases, we do not include these observations in this work. For the ones included, we used a flux calibrator of an adjacent epoch to set the flux density of the secondary calibrator.

All data were processed using the Common Astronomy Software Applications (CASA; McMullin et al. 2007). The `AOflagger` algorithm (Offringa, van de Gronde & Roerdink 2012) was used to flag data corrupted by radio frequency interference. Standard calibration procedures were applied to each observation, and calibration solutions were applied to the target data before imaging. Starting in 2006, the VLA antennas were gradually upgraded to Jansky VLA capabilities, and we therefore found baseline-based calibration solutions using the flux calibrator. The CASA task `clean` was used for imaging, utilizing Briggs weighting with a robust value of 1. Self-calibration was not performed.

To measure the flux densities of V445 Pup, the CASA task `imfit` was used to fit a Gaussian to the nova in each resulting image. In most measurements the width of the Gaussian is allowed to vary, and the integrated flux density was recorded. However, in cases of low signal to noise, the size of the Gaussian was fixed to the size of the synthesized beam. The uncertainty in flux density includes the error from the Gaussian fit added in quadrature with estimates of the uncertainty on the absolute flux calibration (5 per cent of the flux for 1–10 GHz and 10 per cent of the flux for frequencies greater than 10 GHz). In epochs where there is a non-detection, the task `imstat` was used to determine the noise of the image. An upper limit on the flux density is determined as three times the image rms plus the value of the pixel at the target location.

The flux densities of V445 Pup for each frequency band are given in Table 3; the first ten epochs are presented in this paper and others are available in the electronic materials.

3 RESULTS

3.1 Radio light curves

Multifrequency observations, spanning 1.5–43.3 GHz, reveal an unusual radio light curve for the eruption of V445 Pup between 2001 and 2008 presented in Fig. 1. The radio light curve shows four distinct flares throughout its evolution.

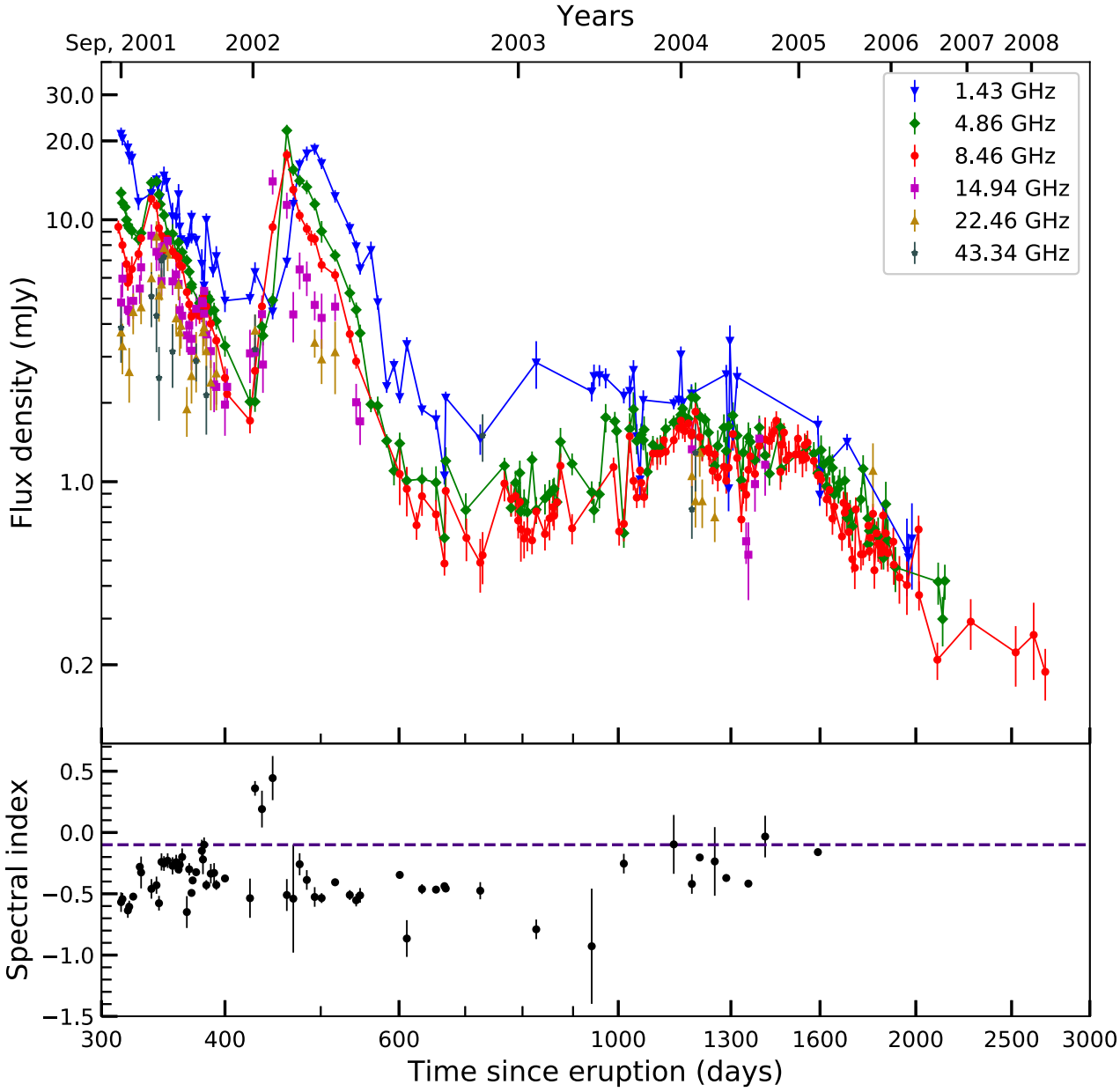

Figure 1. Top: Observed flux densities of V445 Pup spanning from day 300 to day 2700 after the nova eruption. We take 2000 November 2 as the date of the eruption (t_0). Bottom: spectral indices obtained by fitting a single power law to the data. The dashed line in the lower panel represents $\alpha = -0.1$, the theoretically expected index of optically thin free–free emission.

In the earliest radio observation following the eruption of V445 Pup, around day 77, no radio emission was detected, with a 3σ upper limit of 0.34 mJy at 8.4 GHz. However, on day 89, a 4σ detection of 0.35 mJy was obtained at 8.4 GHz. Unfortunately, following the day 89 detection there were no radio observations of the nova until 312 d after eruption. As a result of very limited coverage during the first 300 d after eruption, these early points are not shown in Fig. 1. On day 312, it became clear that V445 Pup had brightened at radio frequencies since day 89 by a factor of ∼26 to 9.4 mJy at 8.4 GHz. Over the next ∼3 months (see Fig. 2), the light curve shows flux densities declining from a radio maximum, which presumably occurred before day 312.

Other flares are superimposed on the decline, like the steep peak on day 337 (at 4.9/8.5/14.9 GHz; Fig. 2). Another flare peaked between days 450 and 460 (at 4.86/8.46/14.94 GHz bands). We note that, for the lowest frequency (1.43 GHz) light curve, these peaks occur later, at days 341 and 493 (Fig. 2).

The radio peaks observed between day 300 and 700, indicated by vertical dashed lines in Fig. 2, have sharp, rapid rises and falls in flux density, compared to the last broad peak which occurs between days 700 and 3000 (Fig. 1). Furthermore, the flux density at the peak of the last flare is a factor of five fainter than the early-time peaks.

The last recorded flux density of the nova with the VLA was 0.19 mJy at 8.46 GHz on 2008 March 29 (day 2704). On 2009 October 29 and December 29 (days 3283 and 3325, respectively), V445 Pup was observed using the Giant Metrewave Radio Telescope (GMRT) at 1.28 and 1.40 GHz (Kantharia 2012). Radio emission was present in the first GMRT observation, with a flux density

Table 2. Log of gain calibrators used at different configurations and observing frequencies.

Observation Date range	Configuration	Gain calibrators 1.43 GHz	4.86 GHz	8.46 GHz	14.94 GHz	22.46 GHz	43.34 GHz
2001 Jan 18–2001 Jan 30	A	...	...	0804-278	...	...	...
2001 Sep 09–2001 Sep 14	C	0738-304	0804-278	0804-278	0804-278	0804-278	0804-278
2001 Sep 15–2001 Oct 10	C&D	0735-175	0804-278	0804-278	0804-278	0804-278	0804-278
		0806-268	0738-304	–	–	–	–
		0706-231	–	–	–	–	–
2001 Oct 12–2002 Jan 13	D	0706-231	0738-304,	0804-278	0804-278	0804-278	0804-278
		0806-268	0804-278	–	–	–	–
2002 Feb 07–2002 Jun 07	A, A&B	0804-278	0804-278	0804-278	0804-278	0804-278	...
2002 Jun 17–2002 Oct 31	B	0804-278	0804-278	0804-278	...	...	0804-278
2002 Dec 09–2003 Jan 29	C, C&D	...	0804-278	0804-278	...	...	...
2003 Feb 06–2003 Apr 18	D	...	0804-278	0804-278	...	...	...
2003 May 30–2003 Oct 08	A, A&B	0735-175	0804-278	0804-278	...	...	...
		0804-278	–	–	–	–	–
2003 Oct 21–2004 Mar 02	B, B&C	0804-278	0804-278	0804-278	0804-278	0804-278	0804-278
2003 Mar 10–2004 June 12	C, C&D	0738-304	0804-278	0804-278	...	0804-278	...
		0706-231					
2004 Jun 25–2004 Aug 21	D	...	0804-278	0804-278	0804-278	...	...
2004 Sep 09–2005 Feb 03	A, A&B	...	0804-278	0804-278	0804-278	...	...
2005 Feb 26–2005 Jul 02	B, B&C	0804-278	0804-278	0804-278	...	...	...
2005 Jul 09–2005 Oct 31	C, C&D	...	0804-278	0804-278	...	0804-278	...
2005 Nov 08–2006 Jan 22	D	...	0738-304	0804-278	...	...	...
2006 Mar 15–2006 May 10	A	...	...	0804-278	...	...	...
2006 Jun 25–2006 Sep 11	B	...	0804-278	0804-278	...	...	...
2007 Sep 30–2008 Jan 17	A&B, B	...	...	0804-278	...	...	...
2007 Jan 23, 2008 Mar 28	C&D, D	...	...	0804-278	...	...	...

Note. '...' indicates no observations at that date range and frequency.

Table 3. Flux densities and spectral indices of V445 Pup.

t (MJD)	$t - t_0$ (d)	Radio flux densities (mJy) 1.43 GHz	4.86 GHz	8.46 GHz	14.94 GHz	22.46 GHz	43.34 GHz	α
51927	77	...	...	< 0.34	...	...	...	...
51939	89	...	...	0.354 ± 0.064	...	...	...	...
52162	312	...	...	9.39 ± 0.54	...	...	...	...
52164	314	21.27 ± 1.22	12.66 ± 0.71	...	4.83 ± 0.82	3.71 ± 0.50	3.87 ± 1.03	-0.57 ± 0.08
52165	315	20.47 ± 1.24	11.59 ± 0.64	8.00 ± 0.54	5.96 ± 0.90	3.29 ± 0.72	...	-0.54 ± 0.05
52167	317	...	11.18 ± 0.62	...	...	...	...	...
52168	318	...	9.99 ± 0.66	6.77 ± 0.45	...	...	...	...
52169	319	18.86 ± 1.24	9.52 ± 0.55	5.74 ± 0.38	4.54 ± 0.57	...	...	-0.64 ± 0.06
52170	320	17.55 ± 1.26	9.30 ± 0.50	6.03 ± 0.41	4.48 ± 0.57	2.62 ± 0.62	...	-0.61 ± 0.05
52173	323	17.25 ± 1.07	9.07 ± 0.62	6.48 ± 0.76	4.90 ± 0.72	4.44 ± 0.79	...	-0.52 ± 0.02
52178	328	11.71 ± 0.82	8.44 ± 0.45	7.40 ± 0.39	5.46 ± 0.69	...	...	-0.28 ± 0.03
52179	329	...	8.89 ± 0.48	8.50 ± 0.46	6.58 ± 0.73	4.63 ± 0.64	...	-0.33 ± 0.13

Note. '...' indicates no measurements for flux density for the epoch at that frequency. This table is continued in Appendix C Table C2.

$\sim 0.3 \pm 0.08$ mJy. The second epoch yields a non-detection with a 3σ upper limit of 60 μJy (Kantharia 2012).

3.2 Radio spectral evolution

We determine the spectral index for each observation (α, defined as $S_\nu \propto \nu^\alpha$, where S_ν is the flux density and ν is the observing frequency), from the slope of the line fit to the data in log–log scale. The python function `curve-fit` in the `scipy` package is used to perform the least-squares fit. Detections separated by less than a day are combined into one spectral index fit. Selected spectra are plotted in Fig. 3, while the lower panel of Fig. 1 shows how the spectral index varies with time.

During the first decay of the radio flux density (days ∼312–400), the spectrum has a form that rises steeply towards low frequencies and is well fit with a single power law. For example, on day 314, $\alpha = -0.6$ (top left-hand panel of Fig. 3), an indication of optically thin synchrotron emission (see Section 4.1 for more discussion). Sometimes the spectrum appears to flatten toward low frequency (such as on day 337) and afterwards the spectrum switches back to being well fit with a single power law (e.g. day 383)

On days 429 and 447, the spectrum becomes inverted and rises towards higher frequencies, with $\alpha \approx 0.4$ (Fig. 3), an indication of optically thick emission. On days 462 and 469, the radio spectrum is transitioning back to an optically thin state, exhibiting a combination of inverted/flat spectral index at lower frequencies and steep spectral index at higher frequencies. By day 493, the radio spectrum has returned to optically thin, hovering around $\alpha \approx -0.5$. We discuss likely causes of these changes in the radio spectrum in Section 4.3.

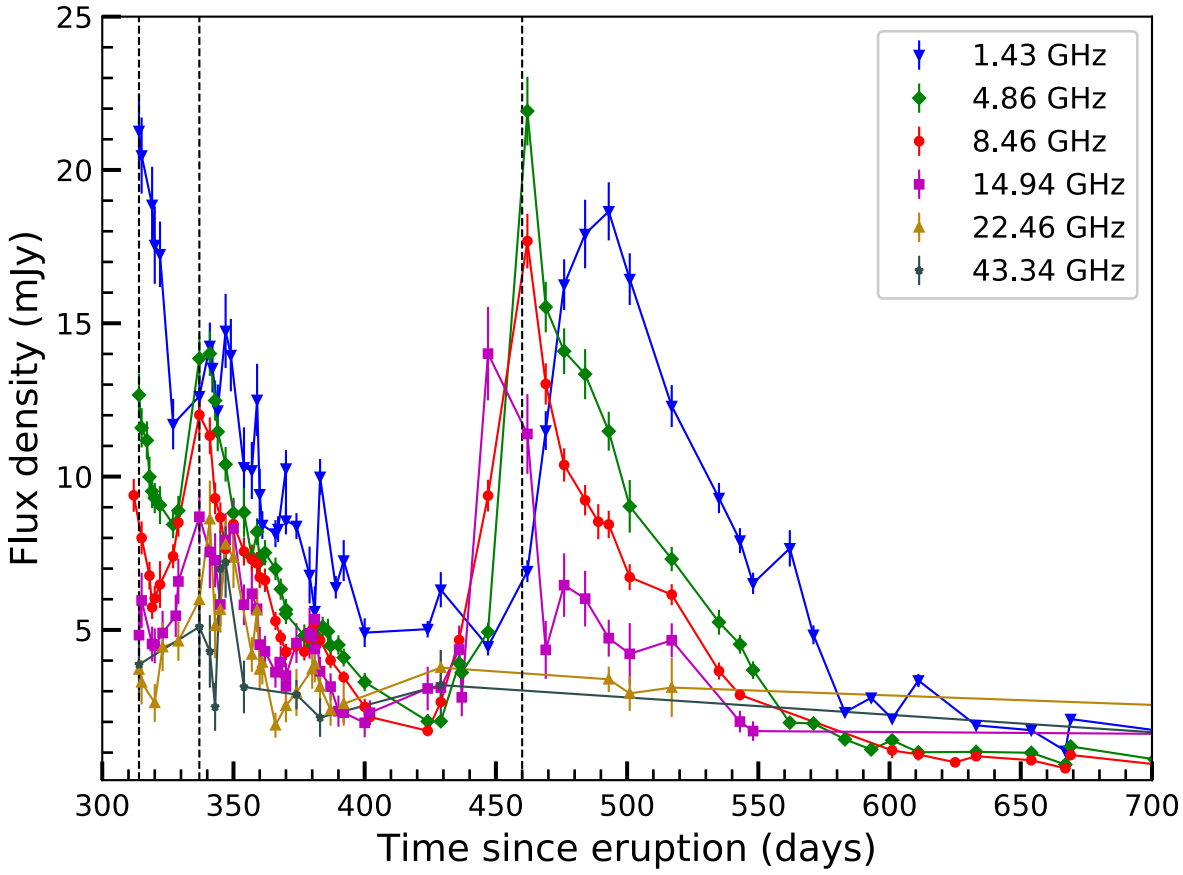

Figure 2. Observed flux densities of V445 Pup spanning from day 300 to day 700 after the nova eruption. Data are the same as those plotted in Fig. 1, but zoomed in to show detail of the radio flares indicated with vertical dashed lines.

3.3 Radio images

In its most extended A configuration, the VLA achieves angular resolution sufficient to constrain the morphology of radio emission from V445 Pup. The dates of these high-resolution observations are listed in Table 4, along with a brief description of the resulting images and the central position of the emission region (more details below). We fit the morphology of V445 Pup in the *uv*-plane, using the UVFIT task in AIPS (Greisen 2003) and DIFMAP (Shepherd, Pearson & Taylor 1994; Shepherd 1997).

The VLA was in A configuration during the first observations of V445 Pup in 2001 January. They yielded a non-detection (January 17, $t - t_0 = 77$ d) and a marginal detection (January 30, $t - t_0 = 89$ d). The S/N was not sufficient to constrain the morphology of V445 Pup at this time.

During the 2002 A configuration (462–559 d after eruption), V445 Pup was radio bright. At 8.4 GHz, it is unresolved; model fitting with an elliptical Gaussian in the *uv* plane implies full width at half-maximum (FWHM) <0.1 arcsec.

During the 2003 A configuration (926–1051 d after eruption), V445 Pup is marginally resolved. We model the 8.4 GHz data in the *uv* plane with an elliptical Gaussian with a major axis of 0.25 ± 0.04 arcsec, unresolved minor axis (<0.1 arcsec), and position angle of 92° ± 14° (degrees east from north). Subtracting this Gaussian in the *uv* plane and imaging the residuals, there is some structure remaining which implies that the source is not fully described as a single Gaussian. The central position of the 2003 emission is near the 2002 position, although not consistent within the formal errors (Table 4). Inspection of the images implies that they likely share a common position, but the more complex morphology of the 2003 image leads to a slight apparent offset.

During the first months of the 2004 A configuration (1408–1488 d after eruption), V445 Pup is resolved into two distinct regions of emission that are roughly aligned with the major axis of the 2003 elliptical Gaussian fit. In the 8.4 GHz observations, the structure of V445 Pup can be fit with two circular Gaussian components separated by 0.22 ± 0.02 arcsec. No significant motion of the components could be seen over ∼4 months of observations. The north-eastern (NE) component's ICRS coordinates are RA = 7h37m56.890s, Dec = −25°56′58.80″, and the coordinates of the south-western (SW) component are RA = 7h37m56.875s, Dec = −25°56′58.88″. The components themselves are marginally resolved, with the NE component's FWHM = 0.16 ± 0.05 arcsec and the SW component measured to have an FWHM = 0.12 ± 0.03 arcsec. The 2004 components are located on either side of the radio emission imaged in 2002/2003, consistent with them moving away from this origin position. The two 2004 components are similar in brightness, with flux densities of 0.7 ± 0.1 mJy (NE) and 0.5 ± 0.1 mJy (SW). The NE component gradually fades while the SW component gradually brightens and remains the only visible component by the end of 2004.

Fig. 4 compares a VLA image produced by stacking the 8.4 GHz observations obtained during the 2004 A configuration with the near-IR high-resolution image, obtained by Woudt et al. (2009) on 2005 March 26 using the NAOS/CONICA adaptive optics system of the VLT. To make the near-IR *K*-band image, we downloaded several *K*-band exposures from the European Southern Observatory (ESO)

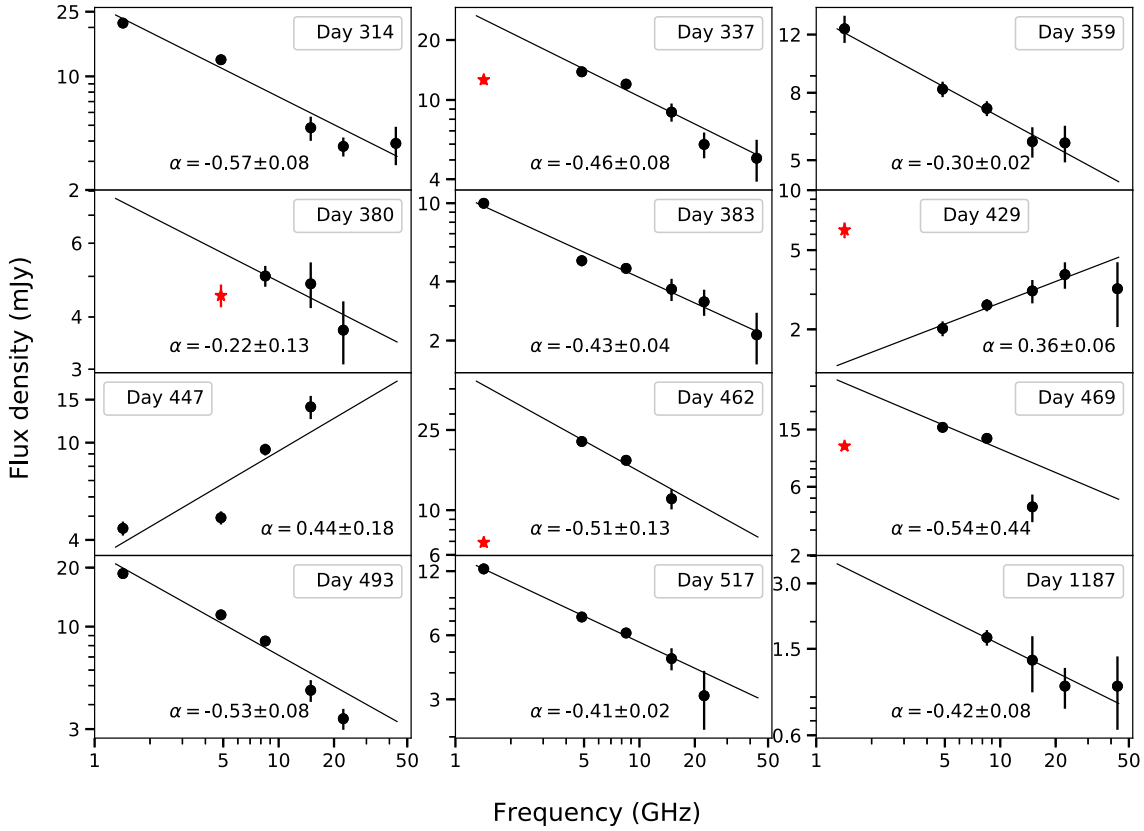

Figure 3. Selected VLA radio spectra of V445 Pup, with linear fits overplotted. The time after eruption (since 2000 November 2) and the value of the spectral index is given for each spectrum. The data points marked with red stars represent flux densities in *L*-band (1.4 GHz) or *C*-band (4.9 GHz) which are relatively flat and thus not included in the fit.

Table 4. High-resolution A-configuration observations of V445 Pup.

Observation Date range	$t - t_0$ (d)	Description	RA (J2000.0) (07h37m56.XXXs)	Dec (J2000.0) ($-25^\circ56'58''.$XX)
2001 Jan 18–Jan 30	77–89	Marginally detected	–	–
2002 Feb 7–May 15	462–559	Unresolved, FWHM <0.1 arcsec	0.885 ± 0.001	0.86 ± 0.01
2003 May 17–Sep 19	926–1051	Marginally resolved, 0.3 × <0.1 arcsec^2	0.880 ± 0.001	0.85 ± 0.02
2004 Sep 23–2005 Jan 6	1408–1526	Two components separated by 0.2 arcsec	NE: 0.890 ± 0.002	0.80 ± 0.03
	–	–	SW: 0.875 ± 0.002	0.88 ± 0.03
2006 Feb 9–May 10	1925–2015	One component, 0.3 × <0.2 arcsec^2	0.883 ± 0.002	0.85 ± 0.04
2007 Jul 15–Jul 28	2446–2459	Marginally detected	–	–

Science Archive Facility (request #543179), stacked them to remove cosmic rays and artefacts, and applied a world coordinate system (WCS) using six stars in the image with *Gaia* Data Release 2 (DR2) positions (estimated error on our WCS is 0.02 arcsec). The near-IR *K*-band emission is a composite of emission lines from warm gas (e.g. He I) and warm dust continuum emission (Woudt et al. 2009).

From Fig. 4, it is clear that the radio emission is emanating from the same bipolar regions of the V445 Pup ejecta that are dominating the near-IR emission. The two images were obtained around the same time (day ∼1445 at 8.4 GHz, and day 1605 at near-IR *K*-band), and to first order, the two radio components are aligned with the peaks of the near-IR emission. Woudt et al. (2009) show that the thermal ejecta expand with a range of velocities in the polar (NE–SW) direction, while expansion in the equatorial plane is confined by a dense dust disc. It is the ejecta nearest to the dust disc that is densest and brightest in the near-IR – and also in radio emission.

We estimate the velocity at which the radio components are travelling apart from one another, assuming they were expelled on t_0 = 51850 MJD and V445 Pup is at a distance of 8.2 kpc. In convenient units, where V is the expansion velocity in km s^{-1} (assumed to be symmetric from a central location), d is in kpc, t is in units of 100 d, and θ is the angular separation in arcsec:

$$V = 8660 \text{ km s}^{-1} \left(\frac{d}{\text{kpc}}\right) \left(\frac{\theta}{\text{arcsec}}\right) \left(\frac{100 \text{ d}}{t}\right). \quad (1)$$

The component separation of 0.22 arcsec on day 1445 implies that the blobs were expanding at 1080 km s^{-1}. If we estimate that both components have FWHM of 0.12 arcsec, then the outer portions of the blobs would be separated by 0.34 arcsec, implying expansion

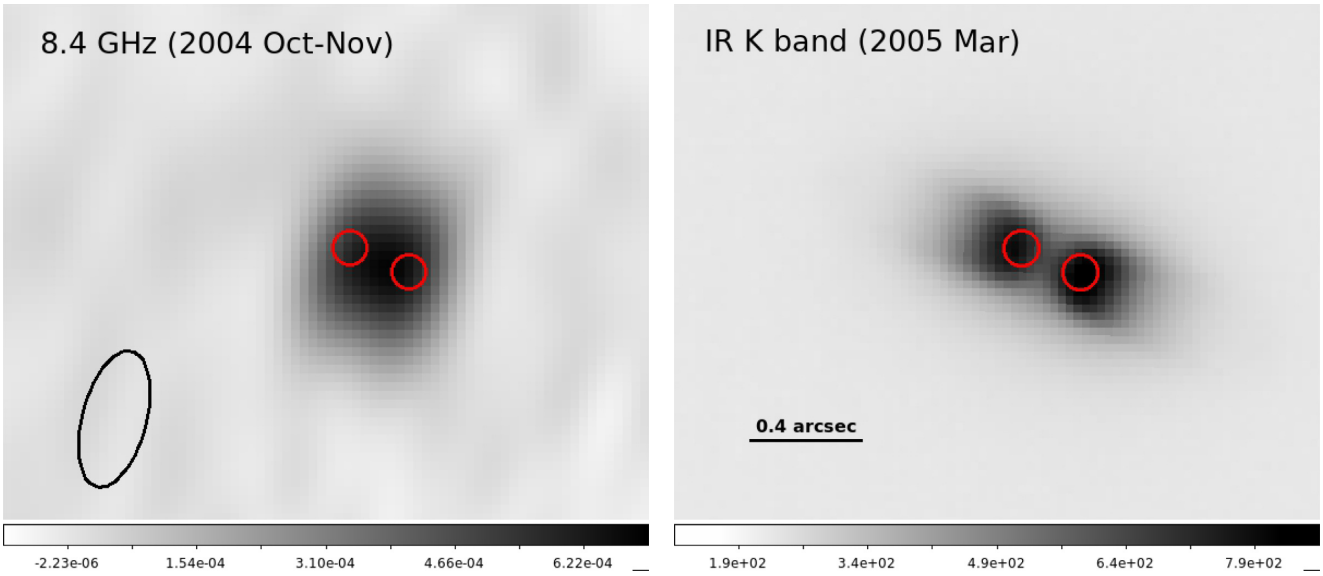

Figure 4. High-resolution images of V445 Pup observed at radio (left-hand panel) and near-infrared (right-hand panel) wavelengths. The red circles are the positions of the two Gaussian components fit to the 2004 October–November A configuration data in the *uv* plane, and have diameters of 0.12 arcsec. The left-hand panel shows our 8.4 GHz image representing the average of data obtained between 2004 September 23 and 2004 November 29 (days 1402–1488). The ellipse in the bottom left-hand corner shows the FWHM extent of the synthesized beam (0.48 × 0.23 arcsec, PA = 165°). The right-hand panel shows a near-IR *K*-band image obtained on 2005 March 26 (day 1605), with the same positions of the radio counterparts marked as red circles. In these images, north is up and east is to the left; and the fields-of-view are matched to be 2.4 × 1.7 arcsec^2. The grey scale is linear in both cases.

velocities of 1670 km s^{-1}. Given these expansion velocities, it is not surprising that we do not observe significant motion during the 2004 A configuration; between 1408 and 1526 d after eruption, we would only expect the two components to move by 0.02–0.03 arcsec – substantially less than our observational errors (Table 4). The velocities of 1000–2000 km s^{-1} implied by the radio imaging are faster than the velocities of the P Cygni absorption troughs observed in optical spectroscopy a few months after eruption (Iijima & Nakanishi 2008), but are slower than the fastest expanding ejecta imaged in the near-IR by Woudt et al. (2009).

We note that the high-velocity infrared 'knots' pointed out at the extremities of the bipolar V445 Pup nebula by Woudt et al. (2009),[1] seen to expand at a remarkable 8450 km s^{-1}, would have been easily resolved in our radio images if they were radio bright. The high-velocity knots are not detected in our 2004 A configuration radio image – a clear demonstration that they are not the source of the bulk of the radio emission ∼1500 d after eruption. Woudt et al. (2009) estimate that the high-velocity knots were ejected 345 d after t_0 (a few months before the 2002 A configuration imaging campaign). If the high-velocity knots had been radio-emitting during our 2003 A configuration campaign, they would have been separated by ∼0.7–0.8 arcsec, easily resolvable with our high-resolution radio images. We therefore conclude that it is not the fastest-expanding material in V445 Pup that is dominating the radio emission at any time. Instead, our radio images imply that it is the densest material that is the site of the radio synchrotron emission.

In the 2006 A configuration (day 1925–2015), V445 Pup has substantially faded, and its morphology has reverted to a similar structure as in 2003 (as best we can tell, given the relatively low S/N). We averaged in the *uv*-plane all 8.4 GHz data obtained in this A configuration, and found the data can be well-described by a single elliptical Gaussian with a major axis of 0.32 ± 0.08 arcsec, unresolved minor axis ($\lesssim$0.2 arcsec), and position angle of 68° ± 42° (degrees east from north). The centre of this emission region is consistent with the position of the 2003 emission; it is located between the 2004 components.

By the time of the 2007 A configuration, V445 Pup had faded too much for its morphology to be constrained by our VLA images.

[1]They are not visible in the *K*-band image presented in Fig. 4; this may be because we did not stack all the exposures from 2005 March 26, and so our image is shallower than the one published by Woudt et al. (2009). We also did not deconvolve the *K*-band image as done by Woudt et al.

4 DISCUSSION

4.1 Radio emission from V445 Pup is synchrotron-dominated

Historically, radio emission from hydrogen-rich classical novae was thought to be dominated by thermal free–free radiation from expanding ionized ejecta (Seaquist & Palimaka 1977; Hjellming et al. 1979; Seaquist & Bode 2008). At early times, while the radio luminosity is increasing, the radio-emitting region is optically thick. As the ejecta expand and drop in density, the radio light curve peaks and turns over, as the radio photosphere recedes through the ejecta and the radio emission transitions to an optically thin state. During the optically thick phase of a thermal-dominated radio light curve, the spectral index α is expected to be equal to 2, as for blackbody emission in the Rayleigh–Jeans long-wavelength limit. When the emitting region is optically thin, the spectral index is flat ($\alpha = -0.1$), as expected for bremsstrahlung emission (e.g. Section 6.2 in Pacholczyk 1970). The radio light curve rise, peak, and decay occur on time-scales of months to years – much slower than the evolution of optical light curves of novae.

The other possible source of nova radio emission is synchrotron radiation. The spectral index for optically thin synchrotron emission is set by the energy spectrum of relativistic electrons; if the number of relativistic electrons per unit energy is $N(E) \propto E^{-p}$, then the spectral

index is $\alpha = (1 - p)/2$. For classic diffusive shock acceleration of relativistic particles, $p = 2 - 2.5$, and so $\alpha = -0.5$ to -0.75 (Bell 1978; Blandford & Ostriker 1978). Indeed, $\alpha \approx -0.7$ is commonly observed in synchrotron-emitting SNe and SN remnants. (Chevalier 1982; Weiler et al. 2002). However, several novae that are strong candidates for synchrotron emitters have unusually shallow spectral indices of $\alpha \approx -0.1$ to -0.5 (Taylor et al. 1987; Eyres et al. 2009; Weston et al. 2016a; Finzell et al. 2018). This could imply shallower energy spectra for relativistic electrons in novae (compared to e.g. SNe), or that the synchrotron emitting region is inhomogeneous in terms of particle density and magnetic field strength (Vlasov, Vurm & Metzger 2016). Optical depth effects could also flatten the spectrum; in the jets of active galactic nuclei, partially self-absorbed synchrotron emission routinely produces flat or inverted spectra of the 'radio core', while the more extended transparent regions of the jet display the usual steep spectrum with $\alpha = -0.7$ (Eckart et al. 1986; Blandford, Meier & Readhead 2019).

The radio spectra of V445 Pup from ∼1 to 4.5 yr after optical discovery generally show higher flux densities at lower frequencies (Fig. 3; with the exception of a few epochs which appear optically thick because of their inverted spectra). Spectral indices of V445 Pup are in the range $\alpha \approx 0$ to -1 (Fig. 1). In the first three years of V445 Pup's evolution, its radio spectral index hovers around $\alpha = -0.5$: slightly shallower than that observed for SNe, but well within expectations of synchrotron emission (especially when taking into account the relatively shallow spectral indices observed for other synchrotron-emitting novae). After day ∼1000, the spectral index flattens to $\alpha \approx -0.2$.

To further constrain the radio emission mechanism, we determine the brightness temperature (T_b; a parametrization of surface brightness). Nova ejecta typically have temperatures $\sim 10^4$ K, as a direct result of the photoionization of the ejecta by the central hot white dwarf (Cunningham, Wolf & Bildsten 2015). We therefore expect the brightness temperature to be $\sim 10^4$ K for a nova in the optically thick thermal phase of its radio evolution. As thermal radio emission transitions to optically thin, the brightness temperature is expected to drop well below 10^4 K (Weston et al. 2016a; Finzell et al. 2018). Synchrotron emission, on the other hand, can reach much higher brightness temperatures, up to $\sim 10^{11}$ K (Readhead 1994). Therefore, if the nova's radio brightness temperature is substantially in excess of 10^4 K, this is a promising indication that it is emitting non-thermal radiation.

To estimate the brightness temperature, we must constrain the angular diameter of the object (θ) and measure its flux density (S_ν). We can then calculate the brightness temperature using the formula:

$$\frac{T_b}{\mathrm{K}} = 1.36 \times \left(\frac{\lambda}{\mathrm{cm}}\right)^2 \times \left(\frac{S_\nu}{\mathrm{mJy}}\right) \times \left(\frac{\theta_a \theta_b}{\mathrm{arcsec}^2}\right)^{-1}, \quad (2)$$

where λ is the observing wavelength, θ_a is the major axis diameter, and θ_b is the minor axis diameter. We can estimate θ if we know the speed at which the nova ejecta are expanding (V; equation 1) as a function of time (t; Seaquist & Bode 2008). We take t as the time since t_0 and estimate the expansion velocity $V = 1600\,\mathrm{km\,s^{-1}}$ along the major axis and $V < 800\,\mathrm{km\,s^{-1}}$ along the minor axis (inferred from radio imaging; Section 3.3). We use the observed flux densities at 1.43 GHz (21 cm), which place the strongest constraints on the brightness temperature (compared to higher frequencies).

As seen in Fig. 5, the brightness temperature of V445 Pup starts high, $\sim 10^7$ K on day ∼300, implying that it is undeniably synchrotron emission. The brightness temperature declines with time, to $\sim 10^5$ K by day ∼600, and finally to $\sim 10^4$ K by day ∼2000. Despite a relatively low (for synchrotron emission) brightness temperature of

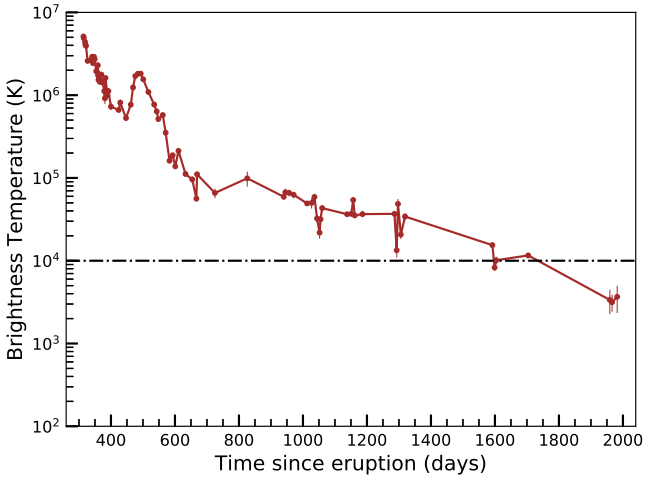

Figure 5. Brightness temperature for V445 Pup between 2001 September and 2006 April.

few $\times 10^4$ K after ∼1000 d, we conclude that this emission is non-thermal, since the spectral index implies that the emission is optically thin. If the emission were optically thin thermal, its brightness temperature should be substantially lower than the $\sim 10^4$ K electron temperature. Therefore, we conclude that the radio light curve of V445 Pup is dominated by synchrotron emission over ∼7 yr of its evolution.

4.2 What powers the synchrotron-emitting shocks in V445 Pup?

The general consensus is that the source of synchrotron emission in novae is due to acceleration of particles to relativistic speeds in shocks. Depending on the nature of the companion star, these shocks can be either external with pre-existing circumbinary material or internal within the ejecta. Which is it for V445 Pup?

The clearest examples of synchrotron emission in hydrogen-rich classical novae come from embedded novae with red giant companions, where external shocks are produced in the interaction of the nova ejecta and the red giant wind. Examples of this type of synchrotron-emitting shocks are RS Oph (O'Brien et al. 2006; Rupen, Mioduszewski & Sokoloski 2008; Sokoloski, Rupen & Mioduszewski 2008; Eyres et al. 2009), V745 Sco (Kantharia et al. 2016), and V1535 Sco (Linford et al. 2017). In these cases, the radio light curve evolves relatively quickly (over ∼weeks), and can be used to trace the radial density profile of the circumbinary material. A late-time thermal radio component is not observed in most cases, indicating that the ejecta are low mass (as expected for the relatively high accretion rates driven by red giant companions; e.g. Yaron et al. 2005).

Another way to produce synchrotron emission could be internal shocks within the ejecta. These type of shocks likely dominate in a white dwarf system whose companion is a main sequence star, and hence the binary system is surrounded by less dense circumbinary material. Such shocks form at the interface of two outflows moving at different speeds, following a nova eruption. For decades there has been evidence of internal shocks in hydrogen-rich classical novae, based on hard X-ray emission (O'Brien, Lloyd & Bode 1994; Mukai & Ishida 2001; Mukai, Orio & Della Valle 2008), and more recently, GeV γ-ray emission (Ackermann et al. 2014; Franckowiak et al. 2018; Martin et al. 2018). It has also recently been recognized

that a significant fraction of these novae show evidence of non-thermal radio emission, manifesting as early bright radio flares. Novae showing evidence of synchrotron emission from internal shocks include QU Vul (Taylor et al. 1987), V959 Mon (Chomiuk et al. 2014), V1723 Aql (Weston et al. 2016a), V5589 Sgr (Weston et al. 2016b), and V1324 Sco (Finzell et al. 2018). These flares rise rapidly with time (∼days–weeks), in contrast to expectations for expanding thermal ejecta (rise time ≈ months), and have brightness temperatures $\gtrsim 10^5 - 10^6$ K. In most cases, a second radio maximum becomes visible at late times which is well-described as expanding thermally emitting ejecta.

Is V445 Pup's radio synchrotron emission driven by external or internal shocks? We know little about the companion star due to dust obscuration (Ashok & Banerjee 2003; Woudt et al. 2009), so it is difficult to predict the properties of the circumbinary material surrounding V445 Pup. We can rule out external shocks with relatively spherically distributed circumbinary material, based on our radio imaging (Section 3.3). If the pre-existing material was isotropically distributed, we would expect the synchrotron emission to be brightest at the fastest shocks (see equation 3), and so to be easily resolvable (as e.g. the near-IR high-velocity knots; Woudt et al. 2009). Instead, the radio emission is confined to much nearer the binary.

Based on radio imaging of V959 Mon, Chomiuk et al. (2014) hypothesize that at the beginning of a nova eruption, a slow outflow concentrated in the equatorial plane of the binary system is generated. A more isotropic fast wind then follows, primarily escaping in the polar directions. The collision between the two distinct flows results in shocks and particle acceleration. Based on near-infrared and radio imaging in the years following the 2000 eruption, V445 Pup exhibits a similar bipolar outflow and an equatorial disc (Woudt et al. 2009). Our radio imaging reveals that the synchrotron emission is concentrated near the equatorial plane, even 3–5 yr after explosion (Section 3.3, Fig. 4). We also know that the equatorial disc maintains its structure for years following the eruption (Woudt et al. 2009). Therefore, interactions between a polar flow and equatorial disc, as proposed for V959 Mon, are the most likely source of the synchrotron emission.

The origin of the equatorial disc, however, is unclear. It may have pre-dated the nova eruption, as mass lost in a previous nova eruption, or from the binary during quiescence (perhaps from the outer Lagrange points during mass transfer; e.g. Pejcha, Metzger & Tomida 2016a). Indeed, from pre-eruption photometry, Woudt et al. (2009) deduced substantial circumbinary dust around V445 Pup in quiescence. The very strong IR signatures of dust early in the eruption led Lynch, Russell & Sitko (2001) to surmise that the dust may have pre-dated the eruption, a conclusion also reached by Shimamoto et al. (2017) when they measured very large dust masses ($\sim 5 \times 10^{-4}$ M$_\odot$) around V445 Pup in 2006. On the other hand, in at least the case of V959 Mon, an equatorial disc-like structure was ejected during the nova eruption itself (Chomiuk et al. 2014; Linford et al. 2015). It is hypothesized that the equatorial structure was produced by the puffed-up nova envelope, marginally bound to the binary shortly after thermonuclear runaway (Chomiuk et al. 2014). As the binary orbited inside the envelope, it transferred energy to help the envelope expand, preferentially in the equatorial direction (i.e. Pejcha, Metzger & Tomida 2016b). It is worth noting that, unlike in V959 Mon, the equatorial disc is not observed to expand or diffuse during the eruption of V445 Pup; it remains present in imaging until at least 2015, and significant dust obscuration persists around the binary up until the present day (Woudt et al., in preparation). This relative constancy of the equatorial disc over ∼ two decades may suggest a pre-eruption origin.

4.3 Understanding the synchrotron-dominated light curve of V445 Pup

The radio synchrotron emission from V445 Pup persists for an unprecedentedly long time (∼7 yr; Fig. 1). Synchrotron emission in other novae lasts for just a few weeks–months (Eyres et al. 2009; Kantharia et al. 2016; Weston et al. 2016a, b; Linford et al. 2017). One relatively simple way to explain the long synchrotron duration of V445 Pup would be if a wind was launched from the binary and continued blowing for years after eruption, while the equatorial disc retained its structure over this time. Then ongoing interactions between the wind and the disc would continue to power synchrotron luminosity. The standard mechanism for driving prolonged winds in novae is radiation pressure from an ∼Eddington luminosity white dwarf, powered by nuclear burning on the white dwarf's surface (Kato & Hachisu 1994). While ∼7 yr is relatively long for this sustained burning phase, it is not unprecedented amongst hydrogen-rich classical novae (Henze et al. 2014). The larger envelope masses in helium novae lead to expectations of longer durations for the sustained burning phase in systems like V445 Pup (∼few yr – 10 000 yr; Kato & Hachisu 2004). Therefore, a wind prolonged over ∼7 yr seems reasonable. Unfortunately, we are not able to directly test if a wind in V445 Pup was powered by the nuclear-burning white dwarf, as no X-ray observations of the eruption are available, and the dusty equatorial disc would likely have absorbed the white dwarf supersoft X-ray emission.

To explain the synchrotron emission from V445 Pup, we consider a cartoon model where the white dwarf wind impacts upon the equatorial disc (we assume the disc is not expanding, as it has appeared largely unchanged in imaging over ∼15 yr post eruption; Woudt et al. 2009, Woudt et al., in preparation). We approximate that the wind expands at 1600 km s^{-1}, based on our radio imaging (Section 3.3), noting that this is the measured velocity in the polar (NE–SW) direction. We take a scenario where a wind of this velocity emanates from the white dwarf isotropically, but is decelerated in the equatorial direction by the disc, creating shocks, accelerating particles, and producing the observed synchrotron emission. We use a simple prescription for synchrotron luminosity, as described in Appendix A and largely taken from Chevalier (1982, 1998). We assume a fraction of the post-shock energy density is transferred to energy density of the amplified magnetic field ($U_{\rm B} = \epsilon_{\rm B} \rho_{\rm disc} v_{\rm w}^2$) and of relativistic electrons ($U_e = \epsilon_e \rho_{\rm disc} v_{\rm w}^2$). Here $\rho_{\rm disc}$ is the density of the pre-shock material and $v_{\rm w}$ is the velocity of the wind, $\epsilon_{\rm B}$ and ϵ_e represent the fraction of the post-shock energy due to amplified magnetic fields and the relativistic electrons, respectively. We note that this is likely an oversimplification if the wind significantly decelerates in the equatorial direction, implying that a reverse shock contributes to the shock luminosity (Metzger et al. 2014). A thorough treatment of V445 Pup's shocks and resultant synchrotron luminosity requires a multidimensional hydrodynamics simulation, so our goal here is only to draw a simple cartoon. When the synchrotron emission is optically thin, its luminosity (L_ν) is proportional to the synchrotron-emitting volume $V_{\rm synch} \times U_e \times U_{\rm B}^{(p+1)/4}$. For V445 Pup, the index of the relativistic electron energy spectrum is measured to be $p \approx 2$ (Section 4.1); therefore

$$L_\nu \propto V_{\rm synch}\, \epsilon_e\, \epsilon_{\rm B}^{3/4}\, \rho_{\rm disc}^{7/4}\, v_{\rm w}^{7/2}. \quad (3)$$

As described in Appendix A, the synchrotron luminosity of V445 Pup can be explained if $\rho_{\rm disc} \approx 10^4$ cm^{-3}.

Higher synchrotron luminosities imply faster shocks and/or higher densities for interaction. Therefore, the variations in synchrotron luminosity observed in V445 Pup's light curve imply variations in

the wind velocity or density of the equatorial disc – or in the optical depth. Synchrotron-dominated light curves of radio transients often show an optically thick rise, where the flux increases as τ drops, and an optically thin decline, usually interpreted as a decline in the density of material being shocked and/or a decline in the shock velocity (e.g. Weiler et al. 2002). V445 Pup is unusual in showing multiple peaks in its light curve (although see the embedded nova V1535 Sco for a similar albeit less dramatic case; Linford et al. 2017).

These flares are accompanied by changes in the optical depth. While most of the time the synchrotron emission appears optically thin (flux density monotonically rising towards lower frequency or $\alpha < 0$), on the rise to radio peaks, the radio spectrum flips to be brighter at higher frequencies (Figs 1 and 3). Between days 429 and 447 (on the rise to the brightest flare observed, peaking on day ∼460), the flux density increases with frequency all the way up to 22.5 GHz, implying $\alpha = 0.2$ to 0.4. On days 337–341 (rising to a slightly fainter peak on day ∼340), the 1.4 GHz point falls substantially below the power-law fit to higher frequencies, implying that absorption is present but milder than on day 429. In both cases, the radio spectrum returns to optically thin at the peak of the radio flare, and thereafter. The observed cyclic change in the radio spectrum of V445 Pup – starting with optically thin emission, then becoming optically thick, then thin, and then thick and thin again – is unusual and challenging to explain (although again, similar sudden, cyclic changes of α are seen in V1535 Sco; Linford et al. 2017). With a few rough calculations, we can exclude the possibility that the optical depth is due to synchrotron self-absorption (Appendix B). The optical depth is therefore due to free–free absorption, and changes in opacity mean that the ionization state of the absorbing material must be changing. The spectrum never reaches the canonical $\alpha = 2$ for free–free absorption, implying that the emission is only partially optically thick – perhaps because the $\tau \approx 1$ photospheres shrink with frequency as expected in a stellar wind (Panagia & Felli 1975; Wright & Barlow 1975) or because the covering factor of the absorbing screen is substantially smaller than unity (e.g. Diaz et al. 2018).

So, what might explain the observed radio flares, and attending changes in free–free opacity? One possibility is that the white dwarf wind is sweeping through the inner parts of the equatorial disc, and encountering density enhancements within it. This would imply that there are at least four regions of enhanced density in the disc, to explain the flares on day <300 (we only captured its decline), day 340, day 460, and day ∼1300 (Fig. 1). Simulations of equatorial discs produced by mass-loss from the outer Lagrangian points of a mass-transferring binary often find structured discs with spiral-like density enhancements (Pejcha et al. 2016a, b). The flux of V445 Pup rose by a factor of ∼10 (from 2 to 22 mJy at 4.9 GHz) between day 430 and 460. According to equation (3), this would imply an increase in density of a factor of ∼4 to explain this flare.

This interpretation is supported by the rapid declines of the radio flares, which we parametrize as $S_\nu \propto t^\beta$; the value of β can give hints on the source of the synchrotron emission. Harris, Nugent & Kasen (2016) performed hydrodynamic simulations of a shock interacting with 'shells' of enhanced density. During impact with a shell, the energy densities in relativistic electrons and magnetic fields increase dramatically, and therefore the radio light curve will peak. However, as the shock propagates to the outer side of the shell, there is no more material to sweep up, particle acceleration ceases, and the energy densities in relativistic electrons and magnetic fields rapidly drop as expected for adiabatic expansion. At this point the radio light curves decline rapidly as $L_\nu \propto t^{-11.5 \text{ to } -9}$ based on their simulations and analytical relations. Considering the declines from the radio flares on days 337 and 462 (see Fig. 2), β is in the range $-10 \lessapprox \beta \lessapprox -9$, consistent with the shell-interaction simulations.

The other possibility is that the velocity of the wind is variable with time, and synchrotron flares are produced when it is faster. To produce a factor of ten increase in synchrotron luminosity requires a factor of ∼2 increase in the wind velocity, according to equation (3). Other nova eruptions have been observed to host multiple outflows with a range of velocities, seen in optical spectra as new absorption features and broadening emission lines (e.g. Jack et al. 2017; Aydi et al. 2019). Aydi et al. (2020) observed rapid changes in γ-ray flux and shock luminosity over the first ∼40 d of V906 Car's 2018 nova eruption, and attributed this to changes in outflow velocity with support from optical spectroscopy. However, the flares observed in V906 Car, and indeed most hydrogen-rich novae, occur over substantially shorter periods than the ∼few years covered by our V445 Pup radio light curve. Perhaps helium nova eruptions evolve more slowly due to their likely larger envelope masses. However, this is difficult to test, as there was essentially no spectroscopic monitoring of V445 Pup during the time window 1–3 yr after explosion, due to very heavy dust obscuration (Ashok & Banerjee 2003; Lynch et al. 2004; Iijima & Nakanishi 2008), and so it is difficult to constrain if or how the wind velocity changed during this time.

In either case – whether it is variations in density or velocity that produce the radio flares – the likely cause of the changes in optical depth is changes in shock luminosity. If much of this shock luminosity is radiated in the ultraviolet band, it can ionize portions of the equatorial disc ahead of it. The higher the shock luminosity, the more ionized material there will be, and the stronger the free–free absorption. The free–free absorption later dissipates, either because this material recombines or because it is swept up by the shock. We prefer the latter explanation, because if the disc material has a density $\sim 10^4$ cm^{-3} (Appendix A), the recombination time should be of the order of a century (Ferland 2003): much longer than the ∼200 d duration of the radio flare.

4.4 Is V445 Pup an SN Ia progenitor system?

As the only helium nova known, V445 Pup is often singled out as an intriguing candidate for a progenitor system to SNe Ia (e.g. Li et al. 2011; Kelly et al. 2014; McCully et al. 2014). The progenitors of SNe Ia have been constrained with radio continuum observations, where the synchrotron-emitting blast wave formalism of Chevalier and collaborators (i.e. Appendix A) is used to place limits on the density and distribution of circumstellar material near the SN site (e.g. Panagia et al. 2006; Chomiuk et al. 2016; Lundqvist et al. 2020). Tested configurations of circumstellar material are usually oversimplistic, with smooth density profiles and spherical symmetry. Therefore interpretations of radio limits for SNe Ia have substantial associated uncertainty.

The fact that V445 Pup's radio light curve is synchrotron dominated and powered by interaction with an equatorial disc that likely pre-dated the nova eruption presents a unique opportunity to predict what a radio light curve of a realistic SN Ia might look like. We had originally hoped that we could simply 'scale up' from nova ejecta energetics to SN ejecta energetics to predict how an SN exploding in a V445 Pup-like progenitor system would appear at radio wavelengths. However, there are two problems with this strategy. First, the synchrotron emission in V445 Pup was likely produced by a prolonged wind that continued to blow and interact with the disc for years – very different from the impulsive yet homologous explosions of SNe. Secondly, while the equatorial disc

apparently withstood the nova eruption of V445 Pup, it is not clear if it would be destroyed by SN Ia ejecta – and on what time-scale.

In the future, hydrodynamic simulations should model the V445 Pup wind/disc system and work to constrain the mass-loss rate of the white dwarf wind and the density profile of the equatorial disc, using our radio light curve as a critical constraint on the dynamics. This would inform the ejecta mass and energetics of the only helium nova known, and also recreate the circumstellar environment of one of the most promising SN Ia progenitor systems. Once the mass, extent, and morphology of the equatorial disc are better constrained, another hydrodynamic simulation could model the interaction of an SN Ia-like explosion with the disc, and make real predictions for observable signatures at radio, optical, and X-ray wavelengths that might indicate a V445 Pup-like progenitor (see Booth, Mohamed & Podsiadlowski 2016 for a similar strategy implemented on another SN Ia progenitor candidate, RS Oph).

5 CONCLUSIONS

The helium nova V445 Pup is observed at radio frequencies for years following its eruption in late 2000 (Fig. 1). Steep spectral indices and high brightness temperatures imply that the radio light curve is powered by synchrotron emission through 2008; we see no evidence of thermal emission from an expanding ionized nova remnant, as seen in many other novae at radio wavelengths. The radio light curve is characterized by at least four re-brightening events, which sometimes are subject to free–free absorption on the rise but revert to optically thin synchrotron emission as they fade. Spatially resolved radio images show that the synchrotron emission is more compact than the thermal ejecta and is confined near the equatorial disc imaged at near-IR wavelengths (Fig. 4).

We hypothesize that a wind from the white dwarf interacts with the equatorial disc, giving rise to shocks, particle acceleration, and synchrotron emission. This model is very similar to the scenario proposed to explain radio synchrotron and GeV γ-ray emission in hydrogen-rich classical nova V959 Mon, also based on radio imaging (Chomiuk et al. 2014). However, the data presented here on V445 Pup present the clearest case to date of synchrotron emission being associated with a dense equatorial disc in a nova. We note that, based on its high synchrotron luminosity and detection of γ-rays in other novae (Ackermann et al. 2014; Franckowiak et al. 2018), V445 Pup was likely a source of substantial GeV γ-rays, but unfortunately its eruption occurred between the *Compton Gamma-Ray Observatory* and *Fermi Gamma-Ray Space Telescope* missions.

The duration of bright synchrotron emission from V445 Pup ($\sim$7 yr) is unprecedented amongst novae. In our model, this implies that the equatorial disc must have maintained its structure throughout these years (a hypothesis directly supported by near-IR imaging of V445 Pup; Woudt et al. 2009). In addition, the wind from the white dwarf must have persisted over these years, which is not surprising if the wind is powered by radiation pressure from sustained burning of helium on the white dwarf's surface (Kato & Hachisu 2004). The re-brightening events in the radio light curve could be produced by changes in wind velocity or density enhancements encountered in the disc, as it is swept up by the wind. Similar fluctuations in shock luminosity have been seen in GeV γ-rays – albeit over shorter time-scales – in the 2018 nova V906 Car (Aydi et al. 2020).

ACKNOWLEDGEMENTS

The authors are grateful to Dr. Chelsea E. Harris and Dr. Ken J. Shen for useful discussions. They also thank Dr. Michael Rupen, Dr. Amy Mioduszewski, and Dr. Vivek Dhawan for their work in obtaining the VLA observations presented here. The National Radio Astronomy Observatory is a facility of the National Science Foundation operated under cooperative agreement by Associated Universities, Inc.

This research was supported by the South African Radio Astronomy Observatory, which is a facility of the National Research Foundation (NRF), an agency of the Department of Science and Innovation. MMN and PAW kindly acknowledge financial support from the University of Cape Town and the NRF. VARMR acknowledges financial support from the Fundação para a Ciência e a Tecnologia (FCT) in the form of an exploratory project (ref. IF/00498/2015/CP1302/CT0001) and the Ministério da Ciência, Tecnologia e Ensino Superior (MCTES) through national and EU funds under the project UIDB/EEA/50008/2020. VARMR is furthermore, supported by the projects Enabling Green E-science for the Square Kilometre Array Research Infrastructure (ENGAGE-SKA, ref. POCI-01-0145-FEDER-022217), and the Origin, composition, evolution and exploration of PHOBOS (ref. POCI-01-0145-FEDER-029932), funded by Programa Operacional Competitividade e Internacionalização (COMPETE 2020) and (FCT), Portugal. LC and KVS acknowledge financial support of National Science Foundation awards AST-1751874 & AST-1907790, NASA grants *Fermi*/80NSSC18K1746 & *NuSTAR*/80NSSC19K0522, and a Cottrell fellowship of the Research Corporation. JS acknowledges support from the Packard Foundation.

Software: CASA (McMullin et al. 2007), AIPS (Greisen 2003), DIFMAP (Shepherd 1997), SCIPY (Oliphant 2007), NUMPY (van der Walt, Colbert & Varoquaux 2011), MATPLOTLIB (Hunter 2007).

DATA AVAILABILITY

The data presented in this work are available through the VLA archive which can be accessed via https://archive.nrao.edu/archive/advquery.jsp.

REFERENCES

Ackermann M. et al., 2014, Science, 345, 554
Ashok N. M., Banerjee D. P. K., 2001, IAU Circ., 7559, 2
Ashok N. M., Banerjee D. P. K., 2003, A&A, 409, 1007
Aydi E. et al., 2019, preprint (arXiv:1903.09232)
Aydi E. et al., 2020, Nat. Astron., 4, 776
Bell A. R., 1978, MNRAS, 182, 147
Bell A. R., 2004, MNRAS, 353, 550
Blandford R. D., Ostriker J. P., 1978, ApJ, 221, L29
Blandford R., Meier D., Readhead A., 2019, ARA&A, 57, 467
Bode M. F., Evans A., 2008, Classical Novae. Cambridge Univ. Press, Cambridge
Booth R. A., Mohamed S., Podsiadlowski P., 2016, MNRAS, 457, 822
Cendes Y., Drout M. R., Chomiuk L., Sarbadhicary S. K., 2020, ApJ, 894, 39
Chevalier R. A., 1982, ApJ, 259, 302
Chevalier R. A., 1998, ApJ, 499, 810
Chevalier R. A., Fransson C., 2006, ApJ, 651, 381
Chomiuk L. et al., 2012, ApJ, 750, 164
Chomiuk L. et al., 2014, Nature, 514, 339
Chomiuk L. et al., 2016, ApJ, 821, 119
Cunningham T., Wolf W. M., Bildsten L., 2015, ApJ, 803, 76
Diaz M. P., Abraham Z., Ribeiro V. A. R. M., Beaklini P. P. B., Takeda L., 2018, MNRAS, 480, L54
Eckart A., Witzel A., Biermann P., Johnston K. J., Simon R., Schalinski C., Kuhr H., 1986, A&A, 168, 17
Eyres S. P. S. et al., 2009, MNRAS, 395, 1533
Ferland G. J., 2003, ARA&A, 41, 517
Finzell T. et al., 2018, ApJ, 852, 108

Franckowiak A., Jean P., Wood M., Cheung C. C., Buson S., 2018, A&A, 609, A120
Greisen E. W., 2003, in Heck A., ed., AIPS, the VLA, and the VLBA. Springer, Dordrecht, p. 109
Harris C. E., Nugent P. E., Kasen D. N., 2016, ApJ, 823, 100
Henze M. et al., 2014, A&A, 563, A2
Hillman Y., Prialnik D., Kovetz A., Shara M. M., 2016, ApJ, 819, 168
Hjellming R. M., Wade C. M., Vandenberg N. R., Newell R. T., 1979, AJ, 84, 1619
Hunter J. D., 2007, Comput. Sci. Eng., 9, 90
Iijima T., Nakanishi H., 2008, A&A, 482, 865
Jack D. et al., 2017, Astron. Nachr., 338, 91
Kantharia N. G., 2012, Bull. Astron. Soc. India, 40, 311
Kantharia N. G. et al., 2016, MNRAS, 456, L49
Kato M., Hachisu I., 1994, ApJ, 437, 802
Kato M., Hachisu I., 2004, ApJ, 613, L129
Kato M., Saio H., Hachisu I., 1989, ApJ, 340, 509
Kato T., Kanatsu K., Takamizawa K., Takao A., Stubbings R., 2000, IAU Circ., 7552, 1
Kelly P. L. et al., 2014, ApJ, 790, 3
Kundu E., Lundqvist P., Pérez-Torres M. A., Herrero-Illana R., Alberdi A., 2017, ApJ, 842, 17
Li W. et al., 2011, Nature, 480, 348
Linford J. D. et al., 2015, ApJ, 805, 136
Linford J. D. et al., 2017, ApJ, 842, 73
Lundqvist P. et al., 2020, ApJ, 890, 159
Lynch D. K., Russell R. W., Sitko M. L., 2001, AJ, 122, 3313
Lynch D. K., Rudy R. J., Mazuk S., Venturini C. C., Puetter R. C., Perry R. B., 2004, AJ, 128, 2962
Martin P., Dubus G., Jean P., Tatischeff V., Dosne C., 2018, A&A, 612, A38
McCully C. et al., 2014, Nature, 512, 54
McMullin J. P., Waters B., Schiebel D., Young W., Golap K., 2007, in Shaw R. A., Hill F., Bell D. J., eds, ASP Conf. Ser. Vol. 376, Astronomical Data Analysis Software and Systems XVI. Astron. Soc. Pac., San Francisco, p. 127
Metzger B. D., Hascoët R., Vurm I., Beloborodov A. M., Chomiuk L., Sokoloski J. L., Nelson T., 2014, MNRAS, 442, 713
Moll R., Woosley S. E., 2013, ApJ, 774, 137
Mukai K., Ishida M., 2001, ApJ, 551, 1024
Mukai K., Orio M., Della Valle M., 2008, ApJ, 677, 1248
Nomoto K., 1982, ApJ, 257, 780
O'Brien T. J., Lloyd H. M., Bode M. F., 1994, MNRAS, 271, 155
O'Brien T. J. et al., 2006, Nature, 442, 279
Offringa A. R., van de Gronde J. J., Roerdink J. B. T. M., 2012, A&A, 539, A95
Oliphant T. E., 2007, Comput. Sci. Eng., 9, 10
Pacholczyk A. G., 1970, Radio Astrophysics. Nonthermal Processes in Galactic and Extragalactic Sources. W. H. Freeman and Co., San Francisco
Panagia N., Felli M., 1975, A&A, 39, 1
Panagia N., Van Dyk S. D., Weiler K. W., Sramek R. A., Stockdale C. J., Murata K. P., 2006, ApJ, 646, 369
Pejcha O., Metzger B. D., Tomida K., 2016a, MNRAS, 455, 4351
Pejcha O., Metzger B. D., Tomida K., 2016b, MNRAS, 461, 2527
Piersanti L., Tornambé A., Yungelson L., Straniero O., 2013, in Di Stefano R., Orio M., Moe M., eds, Proc. IAU Symp. 281, Binary Paths to Type Ia Supernovae Explosions. Cambridge Univ. Press, Cambridge, p. 209
Piersanti L., Tornambé A., Yungelson L. R., 2014, MNRAS, 445, 3239
Readhead A. C. S., 1994, ApJ, 426, 51
Ruiter A. J., Belczynski K., Sim S. A., Seitenzahl I. R., Kwiatkowski D., 2014, MNRAS, 440, L101
Rupen M. P., Dhawan V., Mioduszewski A., 2001, IAU Circ., 7717
Rupen M. P., Mioduszewski A. J., Sokoloski J. L., 2008, ApJ, 688, 559
Sarbadhicary S. K., Badenes C., Chomiuk L., Caprioli D., Huizenga D., 2017, MNRAS, 464, 2326
Seaquist E., Bode M., 2008, Cambridge Astrophys. Ser., 43, 141
Seaquist E. R., Palimaka J., 1977, ApJ, 217, 781
Shen K. J., Bildsten L., 2009, ApJ, 699, 1365
Shepherd M. C., 1997, in Hunt G., Payne H., eds, ASP Conf. Ser. Vol. 125, Astronomical Data Analysis Software and Systems VI. Astron. Soc. Pac., San Francisco, p. 77
Shepherd M. C., Pearson T. J., Taylor G. B., 1994, BAAS, 26, 987
Shimamoto S., Sakon I., Onaka T., Usui F., Ootsubo T., Doi Y., Ohsawa R., Ishihara D., 2017, Publ. Korean Astron. Soc., 32, 109
Sokoloski J. L., Rupen M. P., Mioduszewski A. J., 2008, ApJ, 685, L137
Taylor A. R., Seaquist E. R., Hollis J. M., Pottasch S. R., 1987, A&A, 183, 38
van der Walt S., Colbert S. C., Varoquaux G., 2011, Comput. Sci. Eng., 13, 22
Vlasov A., Vurm I., Metzger B. D., 2016, MNRAS, 463, 394
Weiler K. W., Panagia N., Montes M. J., Sramek R. A., 2002, ARA&A, 40, 387
Weston J. H. S. et al., 2016a, MNRAS, 457, 887
Weston J. H. S. et al., 2016b, MNRAS, 460, 2687
Woosley S. E., Kasen D., 2011, ApJ, 734, 38
Woudt P. A., Ribeiro V. A. R. M. (eds), 2014, ASP Conf. Ser. Vol. 490, Stella Novae: Past and Future Decades. Astron. Soc. Pac., San Francisco
Woudt P. A. et al., 2009, ApJ, 706, 738
Wright A. E., Barlow M. J., 1975, MNRAS, 170, 41
Yaron O., Prialnik D., Shara M. M., Kovetz A., 2005, ApJ, 623, 398

APPENDIX A: SIMPLE MODEL FOR SYNCHROTRON EMISSION FROM NOVAE

Chevalier (1982) developed a simple formalism for interpreting synchrotron emission from stellar explosions. The model was developed for application to SNe, where the ejecta blast wave crashes into pre-existing circumstellar material. The shock between the ejecta and the circumstellar material accelerates particles to relativistic speeds (through diffusive shock acceleration; e.g. Bell 1978; Blandford & Ostriker 1978) and amplifies the magnetic field (through the streaming instability; e.g. Bell 2004). The relativistic electrons gyrate along the magnetic field lines to give rise to synchrotron emission. Here we give a few more details of how this model might be applied to V445 Pup.

The magnetic field strength in the synchrotron-emitting region is simply $B = \sqrt{8\pi U_B}$. The energy density of relativistic electrons is spread between electrons with a power-law distribution of energies, $\mathrm{d}N(E) = N_0 E^{-p}\mathrm{d}E$ where N_0 is a constant, and we assume a minimum energy of relativistic electrons equivalent to the rest mass energy of the electron (Chevalier 1998). We take $p = 2.1$, as measured from the spectrum of V445 Pup (Section 4.1), noting that some of the equations in Chevalier (1998) are not defined for $p = 2.0$.

To convert from a magnetic field strength to physical parameters of the system, we assume a fraction of the post-shock energy density ($\rho_{\rm disc} v_{\rm w}^2$) is converted into amplified magnetic fields and relativistic electrons (as described in Section 4.3). In supernova synchrotron models, conversion factors of $\epsilon_e = \epsilon_{\rm B} = 0.1$ are often assumed (e.g. Chevalier & Fransson 2006; Chomiuk et al. 2012; Cendes et al. 2020). However, recent considerations imply that $\epsilon_{\rm B}$ could be much lower ($\lesssim$0.01; Kundu et al. 2017; Lundqvist et al. 2020), and ϵ_e may also be lower at slower shock velocities (e.g. Sarbadhicary et al. 2017). To roughly estimate the density of material surrounding V445 Pup, we take $\epsilon_e = \epsilon_{\rm B} = 0.01$.

We estimate $V_{\rm synch} \approx 10^{47}\,{\rm cm}^{-3}$, as for a shell that has been expanding for 460 d at 1600 km s^{-1}, with a thickness of 10 per cent. If we take a relatively modest flux density for V445 Pup around this time of 3 mJy at an intermediate frequency of 8.4 GHz (consistent with measurements both before and after the day 460 radio flare), this implies that the shock is interacting with material of density, $\sim$3000 cm^{-3}. Given that this interaction is probably with the equatorial disc, our estimate of a spherical $V_{\rm synch}$ is oversimplistic.

The implied density will increase as the volume filling factor of the synchrotron-emitting material decreases.

APPENDIX B: SYNCHROTRON SELF-ABSORPTION IN V445 PUP?

Could synchrotron self-absorption be the cause of the opacity on the rise to the radio peaks? We can use the flux density at radio peak on day ∼460, combined with a few other rough estimates of system parameters, to estimate the opacity due to synchrotron self-absorption ($\tau_{\rm SSA}$). If synchrotron self-absorption is the dominant source of opacity, we would expect $\tau_{\rm SSA} \approx 1$ at radio peak.

Using the same assumptions described in Appendix A, but instead taking a flux of 12 mJy, we estimate $B = 0.01$ G. We can then plug these quantities into the equation for synchrotron self-absorption optical depth (equation 1 of Chevalier 1998), and find that $\tau_{\rm SSA} \approx 10^{-8}$ at the peak of the day 460 radio flare. As $\tau_{\rm SSA}$ is eight orders of magnitude smaller than unity, we conclude synchrotron self-absorption is not the dominant source of opacity. We note that for $\tau_{\rm SSA} \approx 1$, the emitting volume would need to be $V_{\rm synch} \approx 10^{38}$ cm^{-3}, a factor of a billion smaller than our estimate in Appendix A – but the emitting region is directly constrained by our radio imaging (Section 3.3), and exclude this possibility.

APPENDIX C: VLA OBSERVATIONS OF V445 PUP, MEASURED FLUX DENSITIES AND SPECTRAL INDICES

Table C1. Log of VLA observations of V445 Pup.

Observation date	t (MJD)	$t - t_0$ (d)	Configuration	Observation time on target (min)					
				1.43 GHz	4.86 GHz	8.46 GHz	14.94 GHz	22.46 GHz	43.34 GHz
2001 Oct 4	52187	337	C&D	8.9	6.7	6.7	6.7	6.7	6.2
2001 Oct 8	52191	341	C&D	3.1	4.7	4.7	3.7	5.2	5.4
2001 Oct 10	52193	343	C&D	3.6	4.2	4.2	5.1	5.2	5.6
2001 Oct 12	52195	345	D	2.6	4.1	4.2	5.1	5.2	5.6
2001 Oct 14	52197	347	D	4.4	4.2	4.2	5.7	6.9	6.4
2001 Oct 17	52200	350	D	10.2	4.2	4.2	6.2	7.6	...
2001 Oct 22	52204	354	D	2.9	2.7	2.4	5.2	...	4.7
2001 Oct 24	52207	357	D	4.9	2.7	2.8	6.9	7.6	...
2001 Oct 26	52209	359	D	5.4	5.7	7.4	7.7	7.6	...
2001 Oct 27	52210	360	D	7.3	5.6	7.4	7.7	7.7	...
2001 Oct 29	52212	362	D	4.4	4.7	4.7	6.9	7.4	...
2001 Nov 2	52216	366	D	7.6	8.4	8.6	7.6	7.7	...
2001 Nov 4	52218	368	D	7.8	8.4	24.6	9.2	...	...
2001 Nov 6	52220	370	D	5.9	5.3	5.2	6.2	...	...
2001 Nov 7	52221	371	D	5.9	4.7	4.2	5.8	6.6	...
2001 Nov 11	52224	374	D	6.1	...	4.2	5.3	6.2	5.7
2001 Nov 14	52227	377	D	...	3.9	3.7	...	...	...
2001 Nov 15	52229	379	D	4.1	4.2	2.2	5.1	...	...
2001 Nov 16	52230	380	D	...	5.2	4.9	6.2	6.9	...
2001 Nov 18	52231	381	D	4.2	5.1	3.1	6.2	6.9	...
2001 Nov 20	52233	383	D	4.6	4.2	4.2	6.0	6.9	6.2
2001 Nov 23	52236	386	D	...	4.9	...	...	...	...
2001 Nov 24	52237	387	D	...	4.4	5.1	5.7	7.1	...
2001 Nov 26	52240	390	D	8.1	4.2	...	6.4	...	...
2001 Nov 29	52242	392	D	5.1	5.1	5.4	6.1	7.1	...
2001 Dec 7	52250	400	D	8.2	4.2	4.2	6.2	...	...
2001 Dec 9	52252	402	D	...	...	5.2	6.2	...	...
2001 Dec 31	52274	424	D	5.3	4.2	4.1	6.2	...	...
2002 Jan 5	52279	429	D	7.6	4.2	4.1	6.1	6.7	6.2
2002 Jan 12	52286	436	D	...	4.1	4.2	4.7	...	...
2002 Jan 13	52287	437	D	...	4.1	...	5.6	...	...
2002 Jan 23	52297	447	A	6.4	5.9	7.6	10.6	...	...
2002 Feb 7	52312	462	A	4.2	3.2	9.1	4.7	...	...
2002 Feb 14	52319	469	A	1.9	4.6	10.9	4.7	...	...
2002 Feb 21	52326	476	A	4.1	2.3	6.2	4.7	...	...
2002 Mar 1	52334	484	A	3.9	3.1	7.6	3.7	...	...
2002 Mar 6	52339	489	A	...	...	4.7	...	...	...
2002 Mar 10	52343	493	A	4.6	4.6	9.1	3.7	4.2	...
2002 Mar 18	52351	501	A	2.6	3.2	4.6	3.2	3.2	...
2002 Apr 3	52367	517	A	3.2	5.2	6.1	3.6	3.2	...
2002 Apr 21	52385	535	A	3.2	5.2	6.1	...	...	...
2002 Apr 29	52393	543	A	6.6	5.2	15.3	5.9	...	...
2002 May 4	52398	548	A	6.1	5.2	...	6.1	...	...
2002 May 17	52412	562	A&B	3.3	4.2	...	...	...	...
2002 May 26	52421	571	A&B	3.2	3.1	...	...	...	...

Table C1 – *continued*

Observation date	t (MJD)	$t - t_0$ (d)	Configuration	Observation time on target (min)					
				1.43 GHz	4.86 GHz	8.46 GHz	14.94 GHz	22.46 GHz	43.34 GHz
2002 Jun 7	52433	583	A&B	4.0	3.2	...	...	...	...
2002 Jun 17	52443	593	B	3.6	3.2	...	...	...	...
2002 Jun 25	52451	601	B	3.4	3.2	3.1	..	...	...
2002 Jul 5	52461	611	B	3.4	3.2	3.1	...	...	...
2002 Jul 19	52475	625	B	...	...	16.3	...	...	...
2002 Jul 27	52483	633	B	4.1	3.2	4.7	...	...	...
2002 Aug 17	52504	654	B	4.72	6.2	10.6	...	...	...
2002 Aug 30	52517	667	B	10.6	14.0	13.6	...	...	...
2002 Sep 1	52519	669	B	6.6	8.1	7.9	...	...	...
2002 Oct 4	52552	702	B	...	7.1	7.6	...	...	...
2002 Oct 28	52575	725	B	4.9	4.1	4.2	...	...	...
2002 Oct 31	52579	729	B	...	...	4.1	...	...	4.7
2002 Dec 9	52617	767	C	...	8.2	8.4	...	...	...
2002 Dec 21	52629	779	C	...	6.2	6.1	...	...	...
2002 Dec 29	52637	787	C	...	6.1	6.1	...	...	...
2003 Jan 3	52642	792	C	...	8.1	8.1	...	...	...
2003 Jan 6	52645	795	C	...	8.1	8.2	...	...	...
2003 Jan 8	52647	797	C	...	8.1	8.2	...	...	...
2003 Jan 14	52653	803	C	...	9.2	9.2	...	...	...
2003 Jan 20	52659	809	C	...	9.1	9.1	...	...	...
2003 Jan 29	52668	818	C	...	9.7	9.0	...	...	...
2003 Feb 6	52676	826	D	8.6	9.7	9.1	...	...	...
2003 Feb 23	52693	843	D	...	9.7	9.1	...	...	...
2003 Mar 4	52702	852	D	...	10.4	9.9	...	...	...
2003 Mar 11	52709	859	D	...	10.3	12.2	...	...	...
2003 Mar 13	52711	861	D	...	16.4	22.1	...	...	...
2003 Mar 19	52717	867	D	...	10.4	9.2	...	...	...
2003 Mar 26	52724	874	D	...	10.6	9.2	...	...	...
2003 Apr 18	52748	898	D	...	15.9	12.2	...	...	...
2003 May 30	52790	940	A	8.8	6.9	6.2	...	...	...
2003 Jun 4	52795	945	A	8.6	7.0	...	...	...	...
2003 Jun 16	52807	957	A	8.8	7.7	...	...	...	...
2003 Jun 30	52821	971	A	8.9	7.7	...	...	...	...
2003 Jul 18	52839	989	A	...	...	15.2	...	...	...
2003 Jul 21	52842	992	A	...	15.2	...	...	...	...
2003 Jul 25	52846	996	A	...	16.2	...	...	...	...
2003 Jul 31	52856	1002	A	...	...	9.6	...	...	...
2003 Aug 11	52863	1013	A	8.6	9.2	11.1	...	...	...
2003 Aug 25	52877	1027	A	6.9	9.1	10.7	...	...	...
2003 Sep 3	52886	1036	A	7.3	9.1	18.2	...	...	...
2003 Sep 11	52894	1044	A	10.9	10.1	22.4	...	...	...
2003 Sep 19	52902	1052	A	10.9	...	24.4	...	...	...
2003 Sep	52905	1055	A	8.6	8.1	10.7	...	...	...
2003 Sep 27	52910	1060	A&B	10.8	10.1	...	...	...	...
2003 Sep 29	52912	1062	A&B	...	10.6	11.6	...	...	...
2003 Oct 8	52921	1071	A& B	...	12.2	...	...	...	...
2003 Oct 21	52934	1084	B	...	10.2	14.2	...	...	...
2003 Nov 2	52946	1096	B	...	8.2	8.3	...		
003 Nov 9	52953	1103	B	...	8.7	18.4	...	...	...
2003 Nov 18	52962	1112	B	...	...	14.4	...	...	...
2003 Nov 24	52967	1117	B	...	8.7	10.2	...	...	...
2003 Dec 15	52988	1138	B	5.9	9.1	12.2	...	...	...
2003 Dec 28	53001	1151	B	5.9	9.1	12.2	...	...	...
2004 Jan 3	53007	1157	B	5.1	9.1	12.2	...	...	...
2004 Jan 8	53012	1162	B	5.7	9.2	11.7	...	...	...
2004 Jan 14	53018	1168	B	...	9.2	11.5	...	...	...
2004 Jan 23	53027	1177	B&C	...	6.2	6.4	...	...	...
2004 Feb 1	53036	1186	B&C	5.9	6.2	6.2			
2004 Feb 2	53037	1187	B&C	...	...	4.1	10.3	10.2	10.7
2004 Feb 12	53047	1197	B&C	...	4.2	4.1	...	9.0	10.7
2004 Feb 24	53059	1209	B&C	...	4.2	4.1	...	11.9	...
2004 Mar 2	53066	1216	B&C	...	4.2	4.1	...	12.3	...
2004 Mar 10	53074	1224	C	...	57.4	...	...	...	...

Table C1 – *continued*

Observation date	t (MJD)	$t - t_0$ (d)	Configuration	Observation time on target (min)					
				1.43 GHz	4.86 GHz	8.46 GHz	14.94 GHz	22.46 GHz	43.34 GHz
2004 Mar 20	53084	1234	C	...	4.2	8.1	...	...	...
2004 Mar 22	53086	1236	C	...	...	6.2	...	...	...
2004 Apr 1	53096	1246	C	...	...	8.2	...	...	...
2004 Apr 7	53102	1252	C	...	4.2	8.1	...	13.6	...
2004 Apr 15	53111	1261	C	...	4.2	4.8	...	...	...
2004 May 3	53129	1279	C	...	5.2	8.1	...	...	...
2004 May 10	53136	1286	C	10.6	10.6	9.9	...	...	...
2004 May 17	53143	1293	C& D	10.6	8.9	10.1	...	...	...
2004 May 22	53147	1297	C& D	7.4	...	...	...	...	...
2004 May 30	53156	1306	C& D	6.8	5.2	5.1	...	...	...
2004 Jun 12	53169	1319	C& D	6.0	8.9	10.1	...	...	...
2004 Jun 25	53182	1332	D	...	8.9	10.1	...	...	...
2004 Jul 1	53188	1338	D	...	8.6	10.1	...	...	...
2004 Jul 10	53197	1347	D	...	...	10.1	20.4	...	...
2004 Jul 17	53204	1354	D	...	8.9	10.1	19.2	...	...
2004 Jul 23	53210	1360	D	...	8.6	6.9	....	...	...
2004 Aug 7	53225	1375	D	...	8.9	10.1	12.7	...	...
2004 Aug 21	53239	1389	D	...	9.2	10.2	10.2	...	...
2004 Sep 9	53258	1408	A	...	9.2	10.2	10.2	...	...
2004 Sep 23	53272	1422	A	...	8.6	12.2	...	...	...
2004 Oct 1	53280	1430	A	...	...	18.2	...	...	...
2004 Oct 8	53287	1437	A	...	...	17.4	...	...	...
2004 Oct 16	53295	1445	A	...	...	15.2	...	...	...
2004 Oct 31	53310	1460	A	...	9.1	9.2	...	...	...
2004 Nov 3	53312	1462	A	...	8.2	18.2	...	...	...
2004 Nov 7	53317	1467	A	...	...	14.1	...	...	...
2004 Nov 12	53321	1471	A	...	...	21.1	...	...	...
2004 Nov 20	53329	1479	A	...	...	20.8	...	...	...
2004 Nov 29	53338	1488	A	...	...	21.2	...	...	...
2004 Dec 22	53361	1511	A	...	...	14.6	...	...	...
2004 Dec 31	53370	1520	A	...	...	15.2	...	...	...
2005 Jan 6	53376	1526	A	...	...	13.6	...	...	...
2005 Jan 16	53386	1536	A& B	...	...	10.2	...	...	...
2005 Jan 24	53394	1544	A& B	...	...	8.6	...	...	...
2005 Jan 29	53399	1549	A& B	...	12.1	11.8	...	...	...
2005 Feb 3	53404	1554	A& B	...	...	7.1	...	...	...
2005 Feb 26	53427	1577	B	...	8.6	9.2	...	...	...
2005 Mar 13	53442	1592	B	8.9	8.1	10.3	...	...	...
2005 Mar 20	53449	1599	B	8.8	8.1	10.4	...	...	...
2005 Mar 25	53454	1604	B	8.9	8.1	10.2	...	...	...
2005 Apr 4	53464	1614	B	...	37.7	...	...	...	...
2005 Apr 14	53475	1625	B	...	6.6	8.2	...	...	...
2005 Apr 26	53486	1636	B	...	6.4	9.1	...	...	...
2005 May 6	53497	1647	B	...	5.2	9.0	...	...	...
2005 May 14	53504	1654	B	...	5.1	10.2	...	...	...
2005 May 29	53520	1670	B	...	22.4	...	...	...	...
2005 Jun 3	53525	1675	B	...	19.9	...	...	...	...
2005 Jun 12	53534	1684	B&C	...	...	10.7	...	...	...
2005 Jun 18	53540	1690	B&C	...	...	15.4	...	...	...
2005 Jun 23	53545	1695	B&C	...	13.1	12.2	...	...	...
2005 Jul 2	53554	1704	B&C	11.4	13.1	12.2	...	...	...
2005 Jul 9	53561	1711	C	...	...	4.2	...	...	...
2005 Jul 14	53566	1716	C	...	10.9	...	...	...	...
2005 Jul 23	53575	1725	C	...	10.1	14.2	...	...	...
2005 Aug 2	53585	1735	C	...	...	17.2	...	...	...
2005 Aug 6	53589	1739	C	...	...	6.2	...	...	...
2005 Aug 27	53610	1760	C	...	20.2	12.2	...	...	...
2005 Sep 5	53619	1769	C	...	20.4	16.7	...	...	...
2005 Sep 25	53639	1789	C	...	22.2	...	...	...	...
2005 Sep 27	53641	1791	C	...	12.2	18.2	...	...	...
2005 Oct 1	53645	1795	C	...	20.4	16.7	...	...	...
2005 Oct 5	53649	1799	C&D	...	...	14.4	...	...	...
2005 Oct 16	53660	1810	C&D	...	...	10.4	...	18.7	...
2005 Oct 23	53666	1816	C&D	...	61.6	14.2	...	...	...

Table C1 – *continued*

Observation date	t (MJD)	$t - t_0$ (d)	Configuration	Observation time on target (min) 1.43 GHz	4.86 GHz	8.46 GHz	14.94 GHz	22.46 GHz	43.34 GHz
2005 Oct 31	53675	1825	C&D	...	...	18.4	...	...	...
2005 Nov 8	53683	1833	D	...	9.1	9.2	...	...	...
2005 Nov 15	53690	1840	D	...	...	9.2	...	...	...
2005 Nov 21	53696	1846	D	...	...	21.2	...	...	...
2005 Nov 29	53703	1853	D	...	...	17.4	...	...	...
2005 Dec 1	53705	1855	D	...	13.2	15.6	...	...	...
2005 Dec 11	53715	1865	D	...	13.1	15.6	...	...	...
2005 Dec 20	53724	1874	D	...	13.1	15.2	...	...	...
2006 Jan 13	53748	1898	D	...	...	14.9	...	...	...
2006 Jan 15	53750	1900	D	...	...	18.2	...	...	...
2006 Jan 22	53757	1907	D	...	9.2	...	...	...	...
2006 Feb 9	53775	1925	A	...	...	16.2	...	...	...
2006 Mar 15	53809	1959	A	9.6	...	12.2	...	...	...
2006 Mar 22	53816	1966	A	9.5	...	...	...	...	...
2006 April 7	53832	1982	A	8.9	...	...	...	...	...
2006 May 8	53863	2013	A	...	...	20.2	...	...	...
2006 May 10	53865	2015	A	...	...	14.2	...	...	...
2006 Aug 5	53953	2103	B	...	...	24.6	...	...	...
2006 Aug 9	53957	2107	B	...	24.4	...	...	...	...
2006 Aug 31	53979	2129	B	...	20.6	...	...	...	...
2006 Sep 11	53990	2140	B	...	38.3	...	...	...	...
2007 Jan 23	54123	2273	C&D	...	...	29.3	...	...	...
2007 Sep 30	54374	2524	A&B	...	...	36.0	...	...	...
2008 Jan 17	54482	2632	B	...	...	28.0	...	...	...
2008 Mar 28	54554	2704	C	...	...	10.4	...	...	...

Note. '...' indicates no observations for this epoch at that frequency

Table C2. Flux densities and spectral indices of V445 Pup.

t (MJD)	$t - t_0$ (d)	Radio flux densities (mJy) 1.43 GHz	4.86 GHz	8.46 GHz	14.94 GHz	22.46 GHz	43.34 GHz	α
52187	337	12.62 ± 0.67	13.85 ± 0.71	12.01 ± 0.62	8.69 ± 0.91	5.98 ± 0.88	5.10 ± 1.21	−0.46 ± 0.08
52191	341	14.26 ± 0.76	14.01 ± 0.73	11.33 ± 0.60	7.54 ± 1.17	8.61 ± 1.26	4.30 ± 1.18	−0.43 ± 0.07
52193	343	13.54 ± 0.80	12.48 ± 0.66	9.29 ± 0.52	7.27 ± 0.88	5.13 ± 1.05	2.49 ± 0.78	−0.58 ± 0.06
52195	345	12.15 ± 0.85	11.46 ± 0.63	8.67 ± 0.49	5.83 ± 0.71	5.66 ± 0.75	7.00 ± 1.22	−0.24 ± 0.07
52197	347	14.75 ± 1.21	10.4 ± 0.57	7.64 ± 0.42	7.93 ± 0.87	7.79 ± 0.92	7.21 ± 1.16	−0.25 ± 0.06
52200	350	13.96 ± 1.18	8.81 ± 0.50	8.45 ± 0.46	8.31 ± 0.91	7.36 ± 1.0	...	−0.23 ± 0.06
52204	354	10.30 ± 1.31	8.83 ± 0.79	7.56 ± 0.46	5.82 ± 0.66	...	3.14 ± 0.86	−0.27 ± 0.07
52207	357	10.20 ± 0.93	7.37 ± 0.41	7.30 ± 0.44	6.18 ± 0.68	4.2 ± 0.57	...	−0.24 ± 0.02
52209	359	12.5 ± 1.18	8.2 ± 0.44	7.17 ± 0.37	5.69 ± 0.60	5.64 ± 0.72	...	−0.30 ± 0.02
52210	360	9.42 ± 0.84	7.23 ± 0.40	6.72 ± 0.36	4.52 ± 0.58	3.71 ± 0.69	...	−0.26 ± 0.07
52212	362	8.42 ± 0.45	7.52 ± 0.41	6.62 ± 0.38	4.30 ± 0.51	3.94 ± 0.72	...	−0.20 ± 0.07
52216	366	8.14 ± 0.44	6.99 ± 0.37	5.29 ± 0.30	3.62 ± 0.50	1.89 ± 0.41	...	−0.65 ± 0.13
52218	368	8.29 ± 0.42	6.33 ± 0.35	4.75 ± 0.25	3.95 ± 0.52	...	...	−0.30 ± 0.05
52220	370	10.26 ± 0.61	5.66 ± 0.35	4.28 ± 0.26	3.16 ± 0.49	...	...	−0.49 ± 0.01
52221	371	8.56 ± 0.45	5.52 ± 0.33	4.28 ± 0.26	3.51 ± 0.40	2.53 ± 0.54	...	−0.39 ± 0.02
52224	374	8.39 ± 0.42	...	4.48 ± 0.28	4.57 ± 0.65	2.96 ± 0.77	2.89 ± 0.477	−0.32 ± 0.03
52227	377		...	4.81 ± 0.037	4.29 ± 0.29	...	...	...
52229	379	6.79 ± 0.93	4.68 ± 0.29	4.71 ± 0.35	4.89 ± 0.83	...	...	−0.15 ± 0.09
52230	380	...	4.5 ± 0.28	5.01 ± 0.29	4.80 ± 0.60	3.72 ± 0.64	...	−0.22 ± 0.13
52231	381	5.61 ± 0.81	4.81 ± 0.30	5.25 ± 0.29	4.38 ± 0.54	3.88 ± 0.59	...	−0.10 ± 0.06
52233	383	9.99 ± 0.58	5.10 ± 0.33	4.66 ± 0.26	3.65 ± 0.47	3.15 ± 0.48	2.14 ± 0.63	−0.43 ± 0.04
52236	386	...	4.95 ± 0.41	...	...	...	...	...
52237	387	...	4.49 ± 0.33	4.01 ± 0.26	3.15 ± 0.44	2.39 ± 0.52	...	−0.34 ± 0.08
52240	390	6.39 ± 0.37	4.51 ± 0.32	...	2.35 ± 0.51	...	...	−0.33 ± 0.08
52242	392	12.38 ± 1.08	4.10 ± 0.29	3.46 ± 0.20	2.30 ± 0.33	2.59 ± 0.72	...	−0.43 ± 0.03
52250	400	4.91 ± 0.47	3.30 ± 0.30	2.49 ± 0.26	1.97 ± 0.47	...	...	−0.38 ± 0.03
52252	402	...	...	2.16 ± 0.22	2.30 ± 0.40	...	...	...
52274	424	5.03 ± 0.27	2.02 ± 0.23	1.71 ± 0.18	3.09 ± 0.71	...	...	−0.54 ± 0.16
52279	429	6.31 ± 0.57	2.02 ± 0.17	2.65 ± 0.19	3.12 ± 0.42	3.77 ± 0.57	3.20 ± 1.15	0.36 ± 0.06
52286	436	...	3.91 ± 0.33	4.67 ± 0.33	4.36 ± 0.78	...	...	0.19 ± 0.15

Table C2 – *continued*

t (MJD)	$t - t_0$ (d)	Radio flux densities (mJy) 1.43 GHz	4.86 GHz	8.46 GHz	14.94 GHz	22.46 GHz	43.34 GHz	α
52287	437	...	3.61 ± 0.30	...	2.80 ± 0.62	...	...	...
52297	447	4.46 ± 0.29	4.93 ± 0.31	9.38 ± 0.52	14.01 ± 1.52	...	...	0.44 ± 0.18
52312	462	6.91 ± 0.36	21.92 ± 1.12	17.68 ± 0.89	11.39 ± 1.30	...	...	−0.51 ± 0.13
52319	469	11.49 ± 0.63	15.53 ± 0.83	13.02 ± 0.67	4.35 ± 0.95	...	...	−0.54 ± 0.44
52326	476	16.27 ± 0.83	14.09 ± 0.74	10.38 ± 0.54	6.46 ± 1.04	...	...	−0.26 ± 0.09
52334	484	17.91 ± 1.12	13.34 ± 0.82	9.23 ± 0.50	6.02 ± 0.91	...	...	−0.39 ± 0.08
52339	489	...	...	8.53 ± 0.57	...	...	...	...
52343	493	18.65 ± 0.95	11.48 ± 0.63	8.44 ± 0.45	4.73 ± 0.60	3.39 ± 0.42	...	−0.53 ± 0.08
52351	501	16.44 ± 0.84	9.03 ± 0.86	6.72 ± 0.43	4.22 ± 1.00	2.93 ± 0.57	...	−0.53 ± 0.04
52367	517	12.30 ± 0.68	7.31 ± 0.40	6.15 ± 0.34	4.66 ± 0.55	3.12 ± 0.96	...	−0.41 ± 0.02
52385	535	9.30 ± 0.49	5.25 ± 0.41	3.66 ± 0.28	...	...	...	−0.51 ± 0.04
52393	543	7.91 ± 0.41	4.53 ± 0.30	2.88 ± 0.18	2.01 ± 0.35	...	...	−0.55 ± 0.05
52398	548	6.52 ± 0.35	3.69 ± 0.29	...	1.70 ± 0.32	...	...	−0.51 ± 0.06
52412	562	7.66 ± 0.59	1.97 ± 0.13	...	...	...	...	...
52421	571	4.84 ± 0.31	1.95 ± 0.16	...	...	...	...	...
52433	583	2.32 ± 0.13	1.43 ± 0.09	...	...	...	...	...
52443	593	2.79 ± 0.16	1.10 ± 0.13	...	...	...	...	...
52451	601	2.10 ± 0.11	1.40 ± 0.14	1.07 ± 0.26	...	...	...	−0.35 ± 0.02
52461	611	3.35 ± 0.21	1.01 ± 0.12	0.94 ± 0.20	...	...	...	−0.87 ± 0.15
52475	625	...	...	0.68 ± 0.08	...	...	...	...
52483	633	1.89 ± 0.11	1.02 ± 0.11	0.88 ± 0.14	...	...	...	−0.46 ± 0.04
52504	654	1.73 ± 0.15	0.99 ± 0.15	0.75 ± 0.10	...	...	...	−0.47 ± 0.01
52517	667	1.06 ± 0.08	0.61 ± 0.06	0.49 ± 0.05	...	...	...	−0.44 ± 0.01
52519	669	2.09 ± 0.11	1.20 ± 0.15	0.92 ± 0.17	...	...	...	−0.46 ± 0.00
52552	702	...	0.78 ± 0.12	0.61 ± 0.11	...	...	...	...
52575	725	1.46 ± 0.19	0.89 ± 0.07	0.49 ± 0.11	...	...	...	−0.47 ± 0.07
52579	729	...	...	0.52 ± 0.12	...	...	1.50 ± 0.31	...
52617	767	...	1.15 ± 0.08	0.98 ± 0.14	...	...	...	...
52629	779	...	0.80 ± 0.06	0.86 ± 0.12	...	...	...	...
52637	787	...	0.99 ± 0.11	0.88 ± 0.14	...	...	...	...
52642	792	...	0.85 ± 0.11	0.71 ± 0.10	...	...	...	...
52645	795	...	1.08 ± 0.12	0.84 ± 0.10	...	...	...	...
52647	797	...	0.77 ± 0.11	0.66 ± 0.16	...	...	...	...
52653	803	...	0.84 ± 0.10	0.61 ± 0.10	...	...	...	...
52659	809	...	0.77 ± 0.07	0.65 ± 0.10	...	...	...	...
52668	818	...	1.22 ± 0.09	0.60 ± 0.07	...	...	...	...
52676	826	2.85 ± 0.59	0.78 ± 0.09	0.77 ± 0.07	...	...	...	−0.79 ± 0.08
52693	843	...	0.86 ± 0.11	0.63 ± 0.09	...	...	...	...
52702	852	...	0.90 ± 0.11	0.724 ± 0.13	...	...	...	...
52709	859	...	0.93 ± 0.10	0.80 ± 0.12	...	...	...	...
52711	861	...	0.94 ± 0.09	0.74 ± 0.09	...	...	...	...
52717	867	...	0.84 ± 0.09	0.83 ± 0.10	...	...	...	...
52724	874	...	1.42 ± 0.18	1.15 ± 0.13	...	...	...	...
52748	898	...	1.17 ± 0.11	0.66 ± 0.09	...	...	...	...
52790	940	2.21 ± 0.19	0.91 ± 0.09	0.24 ± 0.04	...	...	...	−0.93 ± 0.47
52795	945	2.53 ± 0.27	0.78 ± 0.08	...	...	...	...	...
52807	957	2.55 ± 0.24	0.90 ± 0.10	...	...	...	...	...
52821	971	2.49 ± 0.22	1.76 ± 0.22	...	...	...	...	...
52839	989	...	...	1.14 ± 0.10	...	...	...	...
52842	992	...	1.7 ± 0.15	...	...	...	...	...
52846	996	...	1.56 ± 0.15	...	...	...	...	...
52852	1002	...	...	0.65 ± 0.08	...	...	...	..
52863	1013	1.69 ± 0.16	1.37 ± 0.10	1.07 ± 0.08	...	...	...	−0.25 ± 0.08
52877	1027	2.22 ± 0.32	1.59 ± 0.23	1.49 ± 0.20	...	...	...	...
52886	1036	2.67 ± 0.24	1.89 ± 0.31	1.01 ± 0.08	...	...	...	...
52894	1044	1.49 ± 0.17	1.43 ± 0.16	0.87 ± 0.08	...	...	...	...
52902	1052	1.02 ± 0.16	...	1.10 ± 0.07	...	...	...	...
52905	1055	1.49 ± 0.16	1.51 ± 0.16	1.00 ± 0.14	...	...	...	...
52910	1060	2.05 ± 0.18	1.44 ± 0.12	...	...	...	...	...
52912	1062	...	1.58 ± 0.20	0.87 ± 0.08	...	...	...	...
52921	1071	...	1.09 ± 0.21	...	...	...	...	...
52934	1084	...	1.38 ± 0.11	1.28 ± 0.13	...	...	...	...
52946	1096	...	1.32 ± 0.16	1.28 ± 0.17	...	...	...	...
52953	1103	...	1.34 ± 0.16	1.28 ± 0.12	...	...	...	...

Table C2 – *continued*

t (MJD)	$t - t_0$ (d)	Radio flux densities (mJy) 1.43 GHz	4.86 GHz	8.46 GHz	14.94 GHz	22.46 GHz	43.34 GHz	α
52962	1112	...	...	1.44 ± 0.15	...	...	...	...
52967	1117	...	1.59 ± 0.15	1.30 ± 0.15	...	...	...	...
52988	1138	1.41 ± 0.25	1.82 ± 0.11	1.46 ± 0.08	...	...	...	−0.10 ± 0.24
53001	1151	2.06 ± 0.10	1.72 ± 0.12	1.60 ± 0.15	...	...	...	...
53007	1157	3.06 ± 0.22	1.80 ± 0.18	1.71 ± 0.18	...	...	...	...
53012	1162	2.01 ± 0.11	1.90 ± 0.20	1.62 ± 0.16	...	...	...	...
53018	1168	...	1.76 ± 0.13	1.56 ± 0.14	...	...	...	...
53027	1177	...	1.74 ± 0.14	1.67 ± 0.15	...	...	...	...
53036	1186	2.17 ± 0.19	2.10 ± 0.21	1.50 ± 0.16	...	...	...	...
53037	1187	...	...	1.54 ± 0.15	1.33 ± 0.38	1.05 ± 0.22	0.78 ± 0.18	−0.42 ± 0.08
53047	1197	...	2.09 ± 0.30	1.85 ± 0.19	...	0.84 ± 0.17	1.29 ± 0.37	...
53059	1209	...	1.53 ± 0.13	1.35 ± 0.12	...	1.14 ± 0.27	...	−0.20 ± 0.02
53066	1216	...	1.33 ± 0.12	1.30 ± 0.10	...	0.84 ± 0.18	...	...
53074	1224	...	1.72 ± 0.10	...	...	...	....	...
53084	1234	...	1.54 ± 0.17	1.34 ± 0.13	...	...	...	...
53086	1236	...	...	1.29 ± 0.15	...	...	...	...
53096	1246	...	...	1.10 ± 0.12	...	...	...	...
53102	1252	...	1.15 ± 0.12	1.27 ± 0.12	...	0.73 ± 0.14	...	−0.24 ± 0.28
53111	1261	...	1.37 ± 0.20	1.04 ± 0.12	...	...	...	...
53129	1279	...	1.61 ± 0.20	1.14 ± 0.15	...	...	...	...
53136	1286	2.27 ± 0.28	1.48 ± 0.10	1.18 ± 0.08	....	...	...	−0.37 ± 0.02
53143	1293	0.94 ± 0.17	1.63 ± 0.20	1.13 ± 0.16	...	...	...	...
53147	1297	3.45 ± 0.50	...	...	...	...	...	...
53156	1306	1.49 ± 0.18	1.79 ± 0.22	1.52 ± 0.18	...	...	...	...
53169	1319	2.51 ± 0.24	1.50 ± 0.16	1.23 ± 0.12	...	...	...	...
53182	1332	...	1.01 ± 0.10	0.72 ± 0.08	...	...	...	...
53188	1338	...	1.29 ± 0.18	0.96 ± 0.13	...	...	...	...
53197	1347	...	...	0.89 ± 0.12	0.59 ± 0.11	...	...	...
53204	1354	...	1.46 ± 0.12	1.17 ± 0.09	0.91 ± 0.19	...	...	−0.42 ± 0.01
53210	1360	...	1.42 ± 0.18	1.25 ± 0.17	...	...	...	...
53225	1375	...	1.21 ± 0.16	1.07 ± 0.12	0.98 ± 0.21	...	...	...
53239	1389	...	1.61 ± 0.18	1.37 ± 0.15	1.46 ± 0.28	...	...	...
53258	1408	...	1.26 ± 0.19	1.45 ± 0.31	1.16 ± 0.28	...	...	−0.03 ± 0.17
53272	1422	...	1.07 ± 0.11	1.43 ± 0.19	...	...	...	...
53280	1430	...	...	1.51 ± 0.19	...	...	...	...
53287	1437	...	...	1.56 ± 0.14	...	...	...	...
53295	1445	...	...	1.71 ± 0.15	...	...	...	...
53310	1460	...	1.61 ± 0.14	1.09 ± 0.16	...	...	...	...
53312	1462	...	1.12 ± 0.12	1.38 ± 0.14	...	...	...	...
53317	1467	...	...	1.39 ± 0.13	...	...	...	...
53321	1471	...	...	1.54 ± 0.13	...	...	...	...
53329	1479	...	...	1.21 ± 0.15	...	...	...	...
53338	1488	...	...	1.26 ± 0.17	...	...	...	...
53361	1511	...	...	1.27 ± 0.19	...	...	...	...
53370	1520	...	...	1.46 ± 0.19	...	...	...	...
53376	1526	...	...	1.27 ± 0.11	...	...	...	..
53386	1536	...	...	1.21 ± 0.17	...	...	...	...
53394	1544	...	...	1.38 ± 0.15	...	...	...	...
53399	1549	...	1.36 ± 0.15	1.23 ± 0.14	...	...	...	...
53404	1554	...	...	1.41 ± 0.16	...	...	...	...
53427	1577	...	1.28 ± 0.14	1.20 ± 0.13	...	...	...	...
53442	1592	1.15 ± 0.12	0.94 ± 0.07	0.87 ± 0.08	...	...	...	−0.16 ± 0.01
53449	1599	0.89 ± 0.08	1.05 ± 0.08	1.06 ± 0.12	...	...	...	...
53454	1604	1.10 ± 0.11	1.32 ± 0.18	1.02 ± 0.16	...	...	...	...
53464	1614	...	1.17 ± 0.09	...	...	...	...	...
53475	1625	...	0.96 ± 0.12	0.86 ± 0.12	...	...	...	...
53486	1636	...	1.21 ± 0.15	0.93 ± 0.11	...	...	...	...
53497	1647	...	1.13 ± 0.14	0.72 ± 0.10	...	...	...	...
53504	1654	...	0.90 ± 0.16	0.80 ± 0.12	...	...	...	...
53520	1670	...	0.94 ± 0.12	...	...	...	...	...
53525	1675	...	0.99 ± 0.12	...	...	...	...	...
53534	1684	...	...	0.62 ± 0.074	...	...	...	...
53540	1690	...	...	0.83 ± 0.09	...	...	...	...

Table C2 – *continued*

t (MJD)	$t - t_0$ (d)	Radio flux densities (mJy) 1.43 GHz	4.86 GHz	8.46 GHz	14.94 GHz	22.46 GHz	43.34 GHz	α
53545	1695	...	1.01 ± 0.13	0.76 ± 0.13	...	...	...	...
53554	1704	1.42 ± 0.10	0.73 ± 0.07	0.81 ± 0.11	...	...	...	...
53561	1711	...	...	0.64 ± 0.08	...	...	...	...
53566	1716	...	0.77 ± 0.08	...	...	...	...	...
53575	1725	...	0.68 ± 0.08	0.51 ± 0.06	...	...	...	...
53585	1735	...	...	0.47 ± 0.08	...	...	...	...
53589	1739	...	...	0.78 ± 0.09	...	...	...	...
53610	1760	...	0.86 ± 0.09	0.53 ± 0.07	...	...	...	...
53619	1769	...	1.12 ± 0.14	0.53 ± 0.05	...	...	...	...
53639	1789	...	0.73 ± 0.08	...	...	...	...	...
53641	1791	...	0.58 ± 0.05	0.68 ± 0.04	...	...	...	...
53645	1795	...	0.65 ± 0.05	0.54 ± 0.05	...	...	...	...
53649	1799	...	...	0.61 ± 0.09	...	...	...	...
53660	1810	...	...	0.75 ± 0.07	...	1.10 ± 0.30	...	...
53666	1816	...	...	0.66 ± 0.06	...	...	...	...
53675	1825	...	...	0.64 ± 0.07	...	...	...	...
53683	1833	...	0.62 ± 0.11	0.58 ± 0.09	...	...	...	...
53689	1840	...	...	0.57 ± 0.08	...	...	...	...
53696	1846	...	...	0.54 ± 0.07	...	...	...	...
53703	1853	...	...	0.74 ± 0.09	...	...	...	...
53705	1855	...	0.51 ± 0.05	0.55 ± 0.05	...	...	...	...
53715	1865	...	0.82 ± 0.18	0.64 ± 0.08	...	...	...	...
53724	1874	...	0.60 ± 0.12	0.53 ± 0.08	...	...	...	...
53748	1898	...	...	0.59 ± 0.08	...	...	...	...
53750	1900	...	...	0.48 ± 0.08	...	...	...	...
53757	1907	...	0.47 ± 0.09	...	...	...	...	...
53775	1925	...	...	0.43 ± 0.09	...	...	...	...
53809	1959	0.54 ± 0.18	...	0.40 ± 0.09	...	...	...	...
53816	1966	0.51 ± 0.12	...	...	...	...	...	...
53832	1982	0.61 ± 0.22	...	...	...	...	...	...
53863	2013	...	...	0.66 ± 0.09	...	...	...	...
53865	2015	...	...	0.37 ± 0.05	...	...	...	...
53953	2103	...	...	0.21 ± 0.03	...	....	...	...
53957	2107	...	0.42 ± 0.08	...	...	...	...	...
53979	2129	...	0.30 ± 0.06	...	...	...	...	...
54123	2273	...	...	0.29 ± 0.06	...	...	...	...
54374	2524	...	...	0.22 ± 0.06	...	...	...	...
54482	2632	...	...	0.26 ± 0.09	...	...	...	...
54554	2704	...	...	0.19 ± 0.04	...	...	...	...

Note. '...' indicates no measurements for flux density for this epoch at that frequency

This paper has been typeset from a TEX/LATEX file prepared by the author.